Apatite as a tracer of the source, chemistry and evolution of ore-forming fluids: the case of the Olserum-Djupedal REE-phosphate mineralisation, SE Sweden

Stefan S. Andersson[a], Thomas Wagner[b], Erik Jonsson[c,d], Tobias Fusswinkel[b], Martin J. Whitehouse[e]

[a]Department of Geosciences and Geography, University of Helsinki, P.O. Box 64 (Gustaf Hällströmin katu 2a), FI-00014 Helsinki, Finland

[b]Institute of Applied Mineralogy and Economic Geology, RWTH Aachen University, Wüllnerstrasse 2, D-52062 Aachen, Germany

[c]Department of Mineral Resources, Geological Survey of Sweden (SGU), Box 670, SE-75128 Uppsala, Sweden

[d]Department of Earth Sciences, Uppsala University, Villavägen 16, SE-75266 Uppsala, Sweden

[e]Swedish Museum of Natural History, Box 50007, SE-10405 Stockholm, Sweden

Corresponding author: Stefan S. Andersson, stefan.andersson@helsinki.fi, +46764269439

Revised version submitted to: Geochimica et Cosmochimica Acta

Date: 10 April 2019

ABSTRACT

This study explores the suitability of apatite as a tracer for the source(s), chemistry, and evolution of ore-forming hydrothermal fluids. This is tested by analysing the halogen (F, Cl, Br, and I), stable Cl isotopic, and trace element compositions of fluorapatite from the regional-scale Olserum-Djupedal rare earth element (REE) phosphate mineralisation in SE Sweden, which is dominated by monazite-(Ce), xenotime-(Y), and fluorapatite. The primary hydrothermal fluid flow system is recorded in a sequence from proximal granite-hosted to distal metasediment-hosted fluorapatite. Along this sequence, primary fluorapatite shows a gradual increase of Cl and Br concentrations and in $(Gd/Yb)_N$, a decrease of F and I concentrations, a decrease in $\delta^{37}Cl$ values, in $(La/Sm)_N$, and partly in $(La/Yb)_N$ and $(Y/Ho)_N$. Local compositional differences of halogen and trace element concentrations have developed along rims and in domains adjacent to fractures of fluorapatite due to late-stage partial reaction with fracture fluids. These differences are insignificant compared to the larger deposit-scale zoning. This suggests that apatite can retain the primary record of the original ore-forming fluid despite later overprinting fluid events. The agreement between Br/Cl and I/Cl ratios of apatite and those of co-existing fluid inclusions at lower temperatures indicates that only a minor fractionation of Br from I occurs during apatite precipitation. The halogen ratios of apatite can thus be used as a first-order estimate for the composition of the ore-forming fluid. Taking the small fractionation factors for Cl isotopes between apatite and co-existing fluid at high temperatures into account, we propose that the Cl isotopic composition of apatite and the halogen ratios derived from the apatite composition can be used jointly to trace the source(s) of ore-forming fluids. By contrast, most trace elements incorporated in apatite are affected by the host rock environment and by fluid-mineral partitioning due to growth competition between co-crystallising minerals. Collectively, apatite is sensitive to changing fluid compositions, yet it is also able to record the character of primary ore-forming fluids. Thus, apatite is suitable for tracing the origin, chemistry, and evolution of fluids in hydrothermal ore-forming settings.

Keywords: Olserum, REE, apatite, fluid tracer, halogens, stable Cl isotopes

1. Introduction

Understanding the sources, chemistry, and evolution of hydrothermal fluids is essential for developing quantitative process models of ore-forming systems. These parameters exert a first-order control on the metal inventory of hydrothermal fluids, the ability to efficiently transport ore metals, and the location where mineral precipitation occurs. Data on the metal and halogen concentrations of hydrothermal ore fluids can be obtained from microanalysis of fluid inclusions (e.g., Seo et al., 2011; Pettke et al., 2012; Hammerli et al., 2014; Wagner et al., 2016; Fusswinkel et al., 2018). The success of quantitative fluid inclusion studies, however, greatly depends on the fluid inclusion record in ore and gangue minerals, which frequently is incomplete or in many cases obliterated, particularly in medium- to high-grade metamorphosed terranes. Thus, utilising the mineral-chemical and isotopic record of common minerals in ore-forming systems that have the potential to preserve the signature of the hydrothermal fluids is an alternative way to obtain such critical data. A variety of minerals have been used for this purpose, such as tourmaline supergroup minerals (e.g., Slack, 1996; Marshall and Jiang, 2011; Slack and Trumbull, 2011; Kalliomäki et al., 2017), zircon (e.g., Valley et al., 2010; Yang et al., 2014), and scapolite group minerals (e.g., Hammerli et al., 2014; Bernal et al., 2017).

True apatites [$Ca_5(PO_4)_3(F,Cl,OH)$], with Br and I in varying proportions (Pan and Fleet, 2002; Pasero et al., 2010), are common in many ore-forming systems, not least in systems rich in rare earth elements (REE; e.g., Frietsch and Perdahl, 1995; Campbell and Henderson, 1997; Rønsbo, 2008; Broom-Fendley et al., 2016a; Chakhmouradian et al., 2017). Apatite is a very versatile mineral as it can incorporate a diverse range of major and trace elements including the halogens in its structure (e.g., Pan and Fleet, 2002; Pasero et al., 2010; Hughes and Rakovan, 2015). The trace element and halogen composition of apatite will reflect the composition of the ore-forming fluid, fluid-mineral partitioning during co-crystallisation with other phases, or compositional features inherited from the host rocks (Belousova et al., 2002; Harlov, 2015; Kusebauch et al., 2015a, 2015b). Not surprisingly, studies utilising apatite to track the composition and evolution of halogens in crustal fluids in a variety of magmatic, metamorphic, sedimentary, and ore-forming environments are abundant (Yardley, 1985; Sisson, 1987;

Boudreau and McCallum, 1989; Zhu and Sverjensky, 1991, 1992; Boudreau et al., 1993; Treloar and Colley, 1996; Hansen and Harlov, 2007; Rasmussen and Mortensen, 2013; Kusebauch et al, 2015a, 2015b; Schisa et al., 2015). The trace element signature of apatite, notably the REE contents, can be used to discriminate between different types of ore deposits (Mao et al., 2016) or to identify the influence of the host rocks and the ore-forming environment on the composition of apatite (Belousova et al., 2002). Moreover, apatite trace element chemistry is particularly suitable in recognising metasomatic processes affecting the mineral after its initial crystallisation (e.g., Harlov et al., 2002, 2005; Harlov and Förster, 2002; Hansen and Harlov, 2007; Harlov, 2015; Zirner et al., 2015; Broom-Fendley et al., 2016a; Jonsson et al., 2016; Krneta et al., 2016). Because Cl is by far the dominant ligand in virtually all ore-forming hydrothermal fluids, determining the stable Cl isotopic composition of apatite can provide key information about the source of fluids and ore metals (Kusebauch et al., 2015a; Barnes and Sharp, 2017).

Most of the studies employing apatite to trace the source, chemistry, or evolution of ore-forming fluids have only utilised the major components substituting on the anionic site in apatite (i.e., F, Cl, and OH) or the trace element compositions. This study employs an expanded and integrated analytical approach and explores the potential of using all the halogens (F, Cl, Br, and I) in conjunction with the stable Cl isotopic (δ^{37}Cl) and trace element compositions of apatite as determined by *in situ* secondary ion mass spectroscopy (SIMS), laser-ablation inductively coupled plasma spectroscopy (LA-ICP-MS), and electron-probe microanalysis (EPMA) techniques. From this data, we evaluate the suitability of apatite as a tracer of the source, chemistry, and evolution of ore-forming fluids with a focus on the regional-scale, hydrothermal Olserum-Djupedal REE-phosphate mineralisation, SE Sweden (Andersson et al., 2018a, 2018b). We propose that the halogen ratios (Br/Cl and I/Cl) and δ^{37}Cl signatures of apatite do largely reflect the primary fluid source and that a combination of halogen and trace element data has the potential to trace the primary hydrothermal fluid and subsequent metasomatic and partly overprinting fluid events.

2. Geological and mineralogical background

2.1. Regional geology

This case study is based on the high-temperature Olserum-Djupedal REE-phosphate mineralisation in the Västervik region in southeast Sweden (Andersson et al., 2018a, 2018b, and references therein). It is hosted by Palaeoproterozoic rocks situated at the border between the Västervik Formation and the granitoid-dominated Transscandinavian Igneous Belt (TIB), south of the Svecofennian domain in the Fennoscandian Shield (Fig. 1; Gavelin, 1984; Gaál and Gorbatschev, 1987; Gorbatschev, 2004). The Svecofennian domain formed during an accretion-type orogeny at 1.92-1.77 Ga (Svecokarelian orogeny). The Västervik Formation is a metasupracrustal unit consisting dominantly of quartzites and meta-arenites deposited in an extensional setting at around 1.88-1.85 Ga (Gavelin, 1984; Beunk and Page, 2001; Sultan et al., 2005). Granitoids and syenitoids of the 1.85-1.65 Ga, NNW-SSE trending TIB complex have intruded the Västervik Formation (Gavelin, 1984; Kresten, 1986; Gorbatschev, 2004; Wikström and Andersson, 2004; Nolte et al., 2011, Kleinhanns et al., 2015). Kleinhanns et al. (2015) suggested that the Palaeoproterozoic domain of the Västervik region represents a southward extension of the tectonic setting proposed for the (Svecofennian) Bergslagen Province located immediately north to northwest of the Västervik region (cf. Stephens et al., 2009, and references therein). This was manifested in the Västervik region by the southwestern migration of a subduction zone and deposition of sediments of the Västervik Formation during an extensional stage. Subsequent changes between extensional and compressional tectonic regimes allowed magmatic rocks of different chemical affinity and origin to form until at least 1.8 Ga (Kleinhanns et al., 2015).

Regional Na ± Ca metasomatism affected the northern and eastern part of the Västervik region (Fig. 1) and is related to granitic magmatism slightly after 1.8 Ga. This event was most likely responsible for the observed alteration and, in part, formation of various styles of U ± REE ± Fe mineralisations in the Västervik region (Uytenbogaardt, 1960; Hoeve, 1974, 1978; Andersson et al., 2018b).

2.2. The Olserum-Djupedal REE-phosphate mineralisation and paragenetic evolution

The presently known Olserum-Djupedal REE-phosphate mineralisation comprises three main areas of exposed REE vein-type mineralisation, namely Olserum, Bersummen, and Djupedal (Fig. 1; Andersson et al., 2018b). Co-existing xenotime-(Y), monazite-(Ce), and fluorapatite are the principal

REE-bearing minerals. These minerals are hosted by biotite-, gedrite-, magnetite, and quartz-dominated veins, vein zones, and pods (Figs. 2A; Andersson et al., 2018b). The veins are mainly hosted by metasedimentary rocks occurring along the margins of a c. 1.8 Ga TIB alkali feldspar granite pluton, which is the dominant rock type. In the Olserum area, where the ore-bearing metasedimentary rocks are well-exposed, they show a transition towards the granite via a zone of intercalated biotite gneisses, granitic to pegmatitic dykes and segregations, and gneissic granites. The veins are also present within this transition zone as well as within the chemically least evolved, and probably earliest, partly gneissic granite in the outermost zone of the pluton. Unmineralised granitic to pegmatitic dykes frequently cross-cut the REE-bearing veins in the Olserum and Bersummen areas, whereas extensive post-ore migmatisation affected the Djupedal area (Andersson et al., 2018a, 2018b).

Detailed petrographic, textural, and mineral chemistry analysis of the main REE-bearing minerals and the associated gangue minerals have demonstrated strong genetic relations between all mineralised areas (Andersson et al., 2018a, 2018b). In combination with field observations, a contact metamorphic-hydrothermal origin for the primary REE mineralisation with monazite-(Ce), xenotime-(Y), REE-bearing fluorapatite and (REE,Y,Th,U,Ca)-(Nb,Ta)-oxide(s) was proposed (Andersson et al., 2018b). The mineralisation was interpreted to have formed at high temperatures (~600 °C) by granite-derived Na-K-rich fluids early in the magmatic evolution within the contact aureole of the TIB granite intrusion.

Primary fluorapatite is the most abundant phosphate in the Olserum-Djupedal REE mineralisation. It is present as large (up to 3-4 cm), white, subhedral to euhedral, and variably recrystallised and fractured crystals, or aggregates of crystals. The primary fluorapatite hosts abundant secondary xenotime-(Y) and monazite-(Ce) inclusions (Andersson et al., 2018a). These inclusions are typically present within the cores of the fluorapatite crystals, whereas the rims, recrystallised grains or domains adjacent to fractures in fluorapatite crystals lack such inclusions (inclusion-absent domains; Figs. 2B, C, and D). The monazite-(Ce) and xenotime-(Y) inclusions formed by early high-temperature dissolution-reprecipitation reactions (e.g., Harlov and Förster, 2003; Harlov et al., 2005, 2016; Harlov, 2015). By utilising a combination of EPMA (La-Sm) and LA-ICP-MS (Eu, Y, and Gd-Lu) mineral-chemical data on monazite-

(Ce) inclusions co-existing with xenotime-(Y), either in direct contact or within the same crystals, monazite-xenotime geothermometry (e.g., Heinrich et al., 1997; Pyle et al., 2001) yielded an average temperature of this early metasomatic alteration of primary fluorapatite of 630 ± 50 °C (Andersson et al., 2018a). The inclusion-absent domains were interpreted to have been formed by leaching of REE+P and subsequent remobilisation (Andersson et al., 2018a). This led to the formation of new xenotime-(Y) and monazite-(Ce) within the surrounding mineral groundmass, within fractures of the fluorapatite crystals, as grains along the rims of the large crystals, and between recrystallised grains (Figs. 2B, C, and D). Locally, a specific textural type of primary fluorapatite is associated with extensively martitised magnetite in the surrounding mineral groundmass (Fig. 2E).

The primary REE-bearing minerals were variably overprinted and altered during subsequent cooling of the hydrothermal system by interaction with late-stage fluids. Remobilised REE, Th, U, and Nb-Ta, formed secondary monazite-(Ce), xenotime-(Y), allanite-(Ce)–ferriallanite-(Ce), uraninite, thorite, and columbite-(Fe) (Andersson et al., 2018a). The alteration involved reaction with a Na-Ca-rich fluid, and locally a very Ca-rich fluid, compared to the ore fluid that precipitated the primary REE-phosphate assemblage. This caused partial to pervasive alteration of monazite-(Ce) and formation of secondary fluorapatite primarily in the ore zone at Djupedal, and the formation of distinct quartz-plagioclase rocks in the surrounding wall rocks (Andersson et al., 2018a, 2018b). Secondary fluorapatite usually replaced monazite-(Ce) along the crystal margins, leaving small relic grains of monazite-(Ce) (Fig. 2F). Later-formed allanite-(Ce)–ferriallanite-(Ce) and minor xenotime-(Y) are also associated with this type of alteration in the Djupedal area. This contrasts with secondary fluorapatite in the Olserum area, where fluorapatite is the only replacement mineral of primary monazite-(Ce) (Andersson et al., 2018a).

REE-mineral formation terminated with the low-temperature (~300 °C) alteration of allanite-(Ce)–ferriallanite-(Ce), which led to the formation of bastnäsite-(Ce) and chlorite ± synchysite-(Ce). This late event overlapped with chloritisation of biotite and magnetite, and the martitisation of primary magnetite (Andersson et al., 2018a).

3. Analytical methods

3.1. Sample selection and preparation

The major and trace element, halogen, and Cl isotopic compositions of fluorapatite of a representative suite of samples (Table 1) from the Olserum-Djupedal REE-phosphate mineralisation were determined by EPMA (major element and Cl and F concentrations), LA-ICP-MS (trace element concentrations), and SIMS (halogen concentrations and Cl isotope compositions). Because of the recognised problem of F and Cl diffusion in apatite due to electron beam exposure (Stormer et al., 1993; Goldoff et al., 2012; Stock et al., 2015), the following analytical protocol was employed to reduce beam exposure of the fluorapatite prior to SIMS and EPMA. Textural relations of selected fluorapatite samples were first studied in thin or thick sections by transmitted and reflected light microscopy and by back-scattered electron (BSE) imaging. From the same sample cut-offs, 25 mm diameter epoxy mounts were prepared for each sample and scanned with a polarisation microscope in high magnification. The mounts were then gold-coated, and SIMS analysis was performed on spots selected beforehand. Halogen concentrations and Cl isotope compositions were measured using different SIMS analytical routines, but the positions of individual spots were placed very close to each other. Prior to coating the samples with carbon for EPMA, the gold-coating was removed, and the mounts were repolished to remove a 5-10 μm thick layer of material from the surface. EPMA was then performed on a spot directly adjacent to the SIMS spots. Admittedly, this procedure cannot fully guarantee that the sampling volume of the different analytical methods exactly corresponds to each other. However, utmost care was exercised when selecting the domains of each grain or crystal that was analysed, making sure that (1) the domains were sufficiently large to accommodate the SIMS spots, the EPMA and the LA-ICP-MS spots, and (2) the individual domains of each grain or crystal were compositionally homogeneous as inferred by initial BSE imaging. BSE images were then acquired to check for compositional homogeneity between the SIMS and EPMA spots. Finally, LA-ICP-MS analysis was performed on the EPMA spot, or directly adjacent to it.

3.2. EPMA

Wavelength-dispersive EPMA was performed on fluorapatite using a JEOL JXA-8600 Superprobe at the University of Helsinki, integrated with the XMAs/IDFix/Diss5 analytical and imaging

software package and SAMx hardware. The following analytical protocol was optimised to minimise the potential effects of F and Cl diffusion in apatite. A beam current of 15 nA, an accelerating voltage of 15 kV, and a beam size of ~15 μm were used for all analyses. Standards, analysed elements, and X-ray lines were as follows: fluorapatite (F-Kα, P-Kα), chlorapatite (Cl-Kα and Ca-Kα), albite (Na-Kα), almandine (Fe-K and Si-Kα), rhodonite (Mn-Kα), and synthetic REE- and Y-phosphates (La-Lα, Ce-Lα, Pr-Lβ, Nd-Lβ, Sm-Lβ, Gd-Lβ, and Y-Lα). Peak and background counting times for REE and Y were 60 s and 30 s, and 30 s and 15 s for the other elements. Calcium, Cl, F, and Na were analysed first on separate spectrometers. When comparing the results from SIMS and EPMA, the Cl concentration data show a good correlation, even for low concentrations (Fig. 3A). Compared to Cl, the data for F do show a considerably larger scatter (Fig. 3B), reflecting the lower precision of F analysis using EPMA. This is due to low count rates and low peak/background ratios. Empirical fluorapatite formulae were calculated based on 12.5 oxygen atoms per formula unit (apfu). X-position occupancies were primarily calculated using F and Cl data from SIMS, and OH was calculated assuming (F + Cl + OH) = 1. This procedure excluded one sample (BER01; Table 1) for which no SIMS halogen data were acquired, and those grains in the other samples where only $\delta^{37}Cl$ was analysed by SIMS.

3.3. LA-ICP-MS

Trace element analysis of fluorapatite using laser-ablation ICP-MS was performed with a Coherent GeoLas MV 193 nm laser-ablation system combined with an Agilent 7900s ICP mass spectrometer at the University of Helsinki. Flow rates of 15 L/min for Ar plasma gas, 0.85 L/min for Ar auxiliary gas, and 1.0 L/min for He carrier gas were used for the analyses. We used an energy density of 5 J/cm^2 and a repetition rate of 10 Hz with 500 laser pulses (equal to 50 s of sample ablation) for each ablation. The following isotopes were measured: ^{23}Na, ^{24}Mg, ^{29}Si, ^{31}P, ^{34}S, ^{35}Cl, ^{42}Ca, ^{43}Ca, ^{45}Sc, ^{51}V, ^{55}Mn, ^{57}Fe, ^{59}Co, ^{75}As, ^{88}Sr, ^{89}Y, ^{139}La, ^{140}Ce, ^{141}Pr, ^{146}Nd, ^{147}Sm, ^{151}Eu, ^{157}Gd, ^{159}Tb, ^{163}Dy, ^{165}Ho, ^{166}Er, ^{169}Tm, ^{172}Yb, ^{175}Lu, ^{208}Pb, and ^{238}U. The concentrations of ^{79}Br or ^{81}Br cannot be quantified because of strong interference of doubly-charged ($^{158}Gd^{++}$ and $^{158}Dy^{++}$) and ($^{162}Dy^{++}$ and $^{162}Er^{++}$) REE species (Fusswinkel et al., 2018), and were consequently not measured. Mass number 150 was measured to

monitor the interference by doubly-charged $^{150}Sm^{++}$ and $^{150}Nd^{++}$ on ^{75}As, and mass 176 to monitor the interference by doubly-charged $^{176}Yb^{++}$, $^{176}Lu^{++}$ and $^{176}Hf^{++}$ on ^{88}Sr. Dwell times used were 0.01 s. Spot analyses of fluorapatite were bracketed with replicate analyses of reference material NIST SRM 610 to correct for instrumental drift and to use as an external standard. The Durango apatite standard was also regularly measured between blocks of unknowns as a control. The concentrations of As, Mn, Pb, (REE+Y), Sr, U, and V are within 15% of the standard values reported for Durango apatite (Chew et al., 2016, and references therein; Table EA1). The accuracy of the LA-ICP-MS data was also checked by daily measurements of the reference material NIST SRM 612 as an unknown sample. The concentrations of most elements measured during the accuracy tests are well within the propagated published uncertainty intervals (Na, Mg, Ca, Mn, Y, Er, and Lu; Spandler et al., 2011), whereas some elements are within or slightly outside these intervals (Sr, La, Ce, Pr, Sm, Eu, Gd, Tm, Yb, Pb, and U; Table EA2). The Ca concentration obtained by EPMA for each individual fluorapatite spot was used as an internal standard (^{43}Ca). For those LA-ICP-MS spots where no EPMA data were acquired, a sample average of Ca concentrations was used (only 24 out of 197 LA-ICP-MS spots). Data handling and calculation of element concentrations were performed with the SILLS software package (Guillong et al., 2008).

3.4. SIMS

The stable Cl isotope composition and halogen concentrations (F, Cl, Br, and I) of fluorapatite were analysed at the NORDSIM facility at the Swedish Museum of Natural History in Stockholm using a Cameca IMS1280 large geometry SIMS instrument. The analytical conditions closely followed those of Marks et al. (2012), Kusebauch et al. (2015a, 2015b), and Bellucci et al. (2017). The halogen concentrations and the Cl isotope compositions were measured using two different analytical routines optimised for each analytical task.

For the halogen concentrations, a primary $^{133}Cs^{+}$ beam with an energy of 20 kV (10 kV primary and -10 kV secondary) was critically focused onto the sample with a 1.2-1.6 nA beam current resulting in a probe diameter of <5 μm. The mass resolving power was set to ~4000 M/ΔM. Prior to analysis, each selected spot was pre-sputtered in a 20 by 20 μm rastered area for 90 s to remove the gold coating and

reduce surface contamination. Following this, the analysis continued with a 10 by 10 μm raster to homogenise the critically-focused beam. A 3000 μm field aperture was used to further minimise surface contamination, limiting the field of view to c. 30 μm. Secondary ion intensities were measured in peak switching mode either on a Faraday cup (for species with counts > 10^6 cps; ^{19}F, ^{35}Cl, and ^{31}P) or low-noise ion-counting electron multiplier (for species with counts < 10^6 cps; ^{81}Br, ^{127}I and the matrix species $^{40}Ca^{31}P$ and $^{40}Ca^{37}Cl$), with five scans acquired over a total integration time of 120 s. At the mass resolving power of ~4000, ^{79}Br and ^{81}Br cannot be adequately resolved from interfering CaCl species. Thus, Br was measured on the combined [^{81}Br + $^{44}Ca^{37}Cl$ + $^{46}Ca^{35}Cl$] mass peak and the interference of the CaCl species was subtracted by using the intensity of the $^{40}Ca^{37}Cl$ peak. All measured peaks were normalised to the $^{40}Ca^{31}P$ matrix signal and concentrations determined relative to the Durango apatite, using halogen concentrations of 33500 ppm F (Marks et al., 2012), 4099 ppm Cl, 0.84 ppm Br, and 0.73 ppm I (Kusebauch et al., 2015b). Detection limits have been estimated to $6.6 \cdot 10^{-5}$ ppm F, $1.3 \cdot 10^{-4}$ ppm Cl, $3.8 \cdot 10^{-3}$ ppm Br, and $7.9 \cdot 10^{-4}$ ppm I (Kusebauch et al., 2015a, 2015b). Replicate measurements (n = 25) of Durango apatite between each block of sample analyses yield a relative standard deviation (RSD, 1σ) of 1% for F, 1.2% for Cl, 11.4% for Br, and 1.5% for I (Table EA3). The calculated RSD's are consistent with previous measurements of the Durango apatite during SIMS analysis at the same facility (Kusebauch et al., 2015a, 2015b; Bellucci et al., 2017).

For Cl isotope analysis, similar analytical conditions as for the halogen measurement were used (primary beam 1.25-1.55 nA, 10 kV, mass resolving power of ~2500, field aperture 3000 μm). Secondary ions of the isotopes ^{35}Cl and ^{37}Cl were collected simultaneously on Faraday cups using multi-collection mode in four blocks of ten integrations (40 cycles) with a total acquisition time of 160 s. Corrections for instrumental drift and matrix-dependent instrumental mass fractionation were made by bracketing the unknown fluorapatite analyses with three to four analyses of the Durango apatite reference material with known isotopic composition ($\delta^{37}Cl$: +0.5‰). A linear correction was applied to the sample fluorapatite isotopic compositions relative to the Durango reference material. The Cl isotopic compositions are expressed using the δ-notation defined as:

$$\delta^{37}Cl = \left[\frac{\left(^{37}Cl/^{35}Cl\right)_{Sample} - \left(^{37}Cl/^{35}Cl\right)_{SMOC}}{\left(^{37}Cl/^{35}Cl\right)_{SMOC}} \right] \cdot 1000\,(‰) \quad (1)$$

where SMOC is the Standard Mean Ocean Chloride with a defined value of 0.0‰ (Kaufmann et al., 1984). The replicate measurements of the Durango apatite (n = 50 during three sessions) yielded an external reproducibility (1σ standard deviation) for δ^{37}Cl of 0.09 to 0.20‰, which is propagated on top of the within-run uncertainty for each analysis.

4. Results

4.1. Major and trace element chemistry of fluorapatite in the Olserum-Djupedal REE-phosphate mineralisation

The analysed fluorapatite types exhibit no systematic compositional differences in CaO and P_2O_5 concentrations, which range from 52.5 to 58.8 wt% CaO and 38.7 to 46.1 wt% P_2O_5 (Table 2; the full mineral chemical data and textural classification is available in the Electronic Supplementary Material, Table EA4). Out of the non-essential elements measured by EPMA, only Fe is consistently present in concentrations above the limit of detection (LOD; about 600 ppm Fe).

The trace elements As, Fe, Mg, Mn, Na, Pb, (REE+Y), Sc, Sr, and U were always detected in fluorapatite during LA-ICP-MS analysis, whereas Co, S, Si, and V were mostly below the LOD (Table 2). Initial tests prior to the final LA-ICP-MS analysis also showed the presence of low but variable concentrations of Ba (< 1.7 ppm), Cd (< 0.5 ppm), Cr (< 3 ppm), Hf (< 0.1 ppm), K (< 1 ppm), Nb (< 1.7 ppm), Ni (< 2 ppm), Sn (< 0.2 ppm), Ti (< 4 ppm), Th (< 6 ppm), and Zn (< 0.7 ppm).

The total concentrations of (REE+Y) range from 0.1 to 0.7 wt%. The (REE+Y) strongly correlate with the Na concentration (Fig. 4), and fluorapatite from the Djupedal area has generally lower Na and (REE+Y) concentrations. The strong correlation indicates that (REE+Y) were mainly incorporated via the following substitution reaction (e.g., Pan and Fleet, 2002):

$$(REE+Y)^{3+} + Na^{+} = 2\,Ca^{2+} \quad (2)$$

The (REE+Y) concentrations show a weak correlation with the Si concentration within individual samples. Scandium and U are also positively correlated with the Na as well as with the (REE+Y) contents.

The REE and Y concentrations were normalised to the average upper continental crust (Rudnick and Gao, 2003). Normalised (REE+Y) distribution patterns show that fluorapatite is enriched in the middle rare earth elements (MREE; Sm to Dy), strongly depleted in the light earth elements (LREE), and relatively enriched in the heavy rare earth elements (HREE). All REE patterns display a distinct negative Eu anomaly and typically also a negative Y anomaly (Fig. 5). All fluorapatite types exhibit similar REE patterns. Yet, the calculated $(La/Sm)_N$, $(La/Yb)_N$, and $(Gd/Yb)_N$ ratios demonstrate clear differences between primary and secondary fluorapatite (Figs. 6A and B). Primary fluorapatite exhibits an increasing enrichment in the MREE, i.e., increasing $(Gd/Yb)_N$ and decreasing $(La/Sm)_N$, and depletion in LREE and HREE in a sequence from granite-hosted fluorapatite towards fluorapatites in the Bersummen and Djupedal areas. The HREE become weakly enriched relative to LREE along this trend as shown by slightly decreasing $(La/Yb)_N$. Secondary fluorapatite defines a separate trend where the LREE increase and the HREE decrease with increasing MREE contents (Fig. 6B). The systematic changes of the REE compositions between the different mineralised areas and between primary and secondary fluorapatites are first-order features of the dataset. By comparison, minor compositional variations are also visible for different domains of primary fluorapatite crystals within individual samples. These are the inclusion-absent domains, i.e., zones in the fluorapatite lacking monazite-(Ce) or xenotime-(Y) inclusions (Figs. 2B, C, and D). These compositional changes typically involve a decrease in the $(Gd/Yb)_N$ ratio and an increase in the $(La/Sm)_N$ ratio in inclusion-absent domains compared to the cores of crystals, whereas the total REE+Y contents show both increasing and decreasing trends. An overview of the first-order compositional features and the changes within individual samples are shown as supplementary figures (Figs. FEA1, FEA2, and FEA3).

Both Fe and Mg are markedly lower in granite-hosted vein fluorapatite compared to metasediment-hosted fluorapatite irrespective of the textural position. Iron and Mg show a strong positive

correlation with each other, and with Co, and to some extent with Pb, (REE+Y), Sc, and U. Out of the other trace elements analysed, Mn, Sr, and Pb show some interesting compositional features. The Mn concentration generally shows a positive correlation with increasing Sr concentration (Fig. 7). The altered primary fluorapatite deviates from this trend and displays a strong negative correlation between Mn and Sr. One group of primary and secondary fluorapatites from the Olserum area also deviate from the general trend and define a separate weak positive trend with higher Mn concentrations (Fig. 7). The altered primary fluorapatite exhibits elevated Sr and Pb concentrations compared to most primary or secondary fluorapatites. Uranium concentrations are always higher in inclusion-absent domains compared to inclusion-rich cores in all primary fluorapatite types, whereas the concentrations of Co, Fe, and Mg are generally lower in the inclusion-absent domains. Of the remaining trace elements, As correlates weakly with increasing Si content. The S and V concentrations range from 100 to 350 ppm and from 0.1 to 3 ppm, respectively, and show no clear correlation with any of the other elements analysed. The Ca, Na, P, S, Si, and V contents show no difference between cores of crystals and inclusion-absent domains, whereas the As, Mn, Pb, and Sc contents either increase or decrease in the inclusion-absent domains.

4.2. Halogen composition of fluorapatite in the Olserum-Djupedal REE-phosphate mineralisation

Granite-hosted vein fluorapatite plots close to the pure end-member and has low Cl concentrations (< 1000 ppm; Table 2). The F concentrations systematically decrease in a sequence from granite-hosted fluorapatite to metasediment-hosted primary fluorapatite in the Olserum area, and then to metasediment-hosted primary fluorapatites in the Bersummen and Djupedal areas (Fig. 8A). The Cl concentrations roughly show an inverse trend. The Cl concentrations of primary fluorapatite from the Olserum area determined in this study are in good agreement with the results of a previous study (Fullerton, 2014). Secondary fluorapatite from the Djupedal area has the highest Cl concentrations, reaching 0.95 wt% (0.13 apfu). This fluorapatite also exhibits a higher calculated OH component resulting from lower F contents. Secondary fluorapatite from the Olserum area is low in Cl (< 2000 ppm). Together with a group of low-Cl primary fluorapatites from the Olserum area, they define a trend of increasing OH-for-F substitution (Fig. 8A). If F is plotted against the $(La/Sm)_N$ ratio (Fig. 8B), the sequence of decreasing F and, in part,

353 increasing Cl concentrations for primary fluorapatite is readily visible. This trend is robust even if the
354 minor compositional differences between fluorapatite cores and inclusion-absent domains are considered.
355 For most primary fluorapatite, F is higher, and Cl is lower in inclusion-absent domains compared to
356 inclusion-rich core domains of the crystals. Only the primary fluorapatite from the Bersummen area
357 deviates from this general trend, with F being lower in the inclusion-absent domains. This is probably
358 coupled with an increase in the OH component because the Cl concentrations show no difference between
359 the fluorapatite cores and inclusion-absent domains (Fig. 8A).

360 Bromine and iodine do also substitute for the major anions in the X-site of apatite, albeit in very
361 low concentrations (e.g., Pan and Fleet, 2002; Kusebauch et al., 2015a). The Br and I concentrations of
362 fluorapatite from the Olserum-Djupedal REE-phosphate mineralisation as measured by SIMS are
363 summarised in Table 2. The variability in Br concentrations is primarily locality-dependent, featuring
364 rather low concentrations in fluorapatite from the Olserum area, whereas both primary and secondary
365 fluorapatites in the Djupedal area, as well as the altered primary fluorapatite, have somewhat higher Br
366 concentrations (Fig. 8C). The I concentration is largely below 1 ppm for all fluorapatite types with a
367 tendency towards slightly lower I concentrations in fluorapatite from the Djupedal area. By comparing
368 crystal cores and inclusion-absent domains, no obvious trend is detectable for Br or I in primary
369 fluorapatite in the Olserum area, whereas Br is lower and I slightly higher in inclusion-absent domains in
370 primary fluorapatite from the Djupedal area. Bromine and iodine were not analysed in primary
371 fluorapatite from the Bersummen area.

372 **4.3. Cl isotopic composition of fluorapatite in the Olserum-Djupedal REE-phosphate mineralisation**

373 The Cl isotope composition shows systematic differences between samples and fluorapatite types
374 (primary and secondary), which are independent of textural features, as the δ^{37}Cl values of crystal cores
375 and inclusion-absent domains are identical within errors. Granite-hosted vein fluorapatite exhibits the
376 highest δ^{37}Cl values, which range between -0.4‰ and +1.6‰. The δ^{37}Cl values then systematically
377 decrease in a sequence from granite-hosted fluorapatite to metasediment-hosted primary fluorapatite in
378 the Olserum area, to metasediment-hosted primary fluorapatites in the Bersummen and Djupedal areas

(Figs. 9, 10A, and B). The $\delta^{37}Cl$ values of secondary fluorapatite in the Djupedal area increase slightly again, ranging between about -0.7‰ and +0.3‰, and secondary fluorapatite from the Olserum area has even higher values, up to +1.0‰. As the $\delta^{37}Cl$ values decrease in the described sequence between mineralised areas, the F and I concentrations, $(La/Sm)_N$, and $(La/Yb)_N$ decrease, whereas the Cl and Br concentrations and $(Gd/Yb)_N$ increase.

5. Discussion

5.1. The sequence of fluorapatite formation in the Olserum-Djupedal REE-phosphate mineralisation

Based on the textural relations and compositional variations, we have recognised four fluid events recorded by fluorapatite: (1) crystallisation of primary ore-stage fluorapatite concomitant with monazite-(Ce) and xenotime-(Y), (2) subsequent modification of primary fluorapatite after initial formation via high-temperature dissolution-reprecipitation reactions, (3) later, lower-temperature remobilisation of REE, and (4) late-stage replacement of monazite-(Ce) and formation of secondary fluorapatite.

The primary fluorapatite records compositional zoning on the deposit-scale in a sequence from granite-hosted fluorapatite to metasediment-hosted primary fluorapatite in the Olserum area, to metasediment-hosted fluorapatites in the Bersummen and Djupedal areas. Fluorapatite shows a distinct increase in Cl and Br concentrations and MREE (decreasing $(La/Sm)_N$ and increasing $(Gd/Yb)_N$), and a decrease in F and I concentrations, as well as in LREE and HREE (LREE more so than the HREE; $(La/Yb)_N$ decreases), and $\delta^{37}Cl$ values along this sequence (Figs. 6, 8, and 10).

The incorporation of halogens into apatite is not only governed by the relative concentrations of the four halogens in the apatite-precipitating fluid at any given conditions of ore-formation (mainly temperature, pressure, pH, and fluid-rock ratio), but also by growth competition with co-crystallising phases such as biotite (Zhu and Sverjensky, 1991; Webster et al., 2009; Doherty et al., 2014; Kusebauch et al., 2015b, Webster and Piccoli, 2015). It is known that F strongly partitions into apatite from F-Cl bearing fluids, even at relatively low HF activities (Zhu and Sverjensky, 1991; Spear and Pyle, 2002;

Harlov, 2015; Kusebauch et al., 2015a, 2015b). Because of the dominance of fluorapatite and the presence of F-rich ore-associated biotite (Andersson et al., 2018b) in the Olserum-Djupedal REE-phosphate mineralisation, the primary ore-forming fluid was clearly both Cl- and F-bearing. The first apatite forming from such a fluid should be essentially pure fluorapatite, as in the case in the granite-hosted fluorapatite. Apatite precipitation would result in progressive F consumption and a decrease in F/Cl ratio in the fluid along the flow path. The apatite precipitating from a more evolved fluid should thus be increasingly Cl-richer if Cl partitioning into apatite is mainly controlled by the chemistry of the fluid.

The Cl concentration in fluorapatite increases from the granite-hosted veins (~0.1 wt% Cl) towards the metasediment-hosted fluorapatite (~0.53 wt% Cl). We thus suggest that the systematic changes in the composition of primary fluorapatite are the product of hydrothermal fluid migration out from the granitic TIB type intrusion into the metasediments. Biotite, which is the other major halogen host phase in the Olserum-Djupedal REE-phosphate mineralisation, also records systematically decreasing $\log(f_{HF}/f_{HCl})$ values from the proximal granite-hosted biotite to the distal metasediment-hosted biotites in the Bersummen and Djupedal areas (Andersson et al., 2018b). The close agreement between changes in biotite and fluorapatite chemistry is consistent with the interpretation that the evolving fluid chemistry exerts the first-order control on the Cl partitioning into fluorapatite and biotite. Increasing Ca content of the fluid towards the Djupedal area (Andersson et al., 2018b) is also consistent with a fluid-chemical control on the uptake of Cl into fluorapatite as Ca-rich fluids promote the uptake of Cl over F in apatite (Harlov and Förster, 2003). In contrast, Kusebauch et al. (2015b) showed a pH-dependent control on the incorporation of Cl into apatite during dissolution-reprecipitation experiments due to the larger compatibility of OH in apatite as compared to Cl. For the fluorapatite of the Olserum-Djupedal REE-phosphate mineralisation, the calculated amount of the OH component is essentially the same for all primary fluorapatites (Fig. 8A), suggesting that the pH had only a minor or negligible effect on the uptake of Cl.

The second fluid event recorded by fluorapatite is the modification through high-temperature dissolution-reprecipitation reactions. This process caused leaching of (REE+Y) from primary fluorapatite

and precipitation of monazite-(Ce) and xenotime-(Y) inclusions inside primary fluorapatite. We suggest that this presumably autometasomatic event occurred shortly after the formation of primary fluorapatite, in a similar fashion as reported for iron oxide-apatite deposits (e.g., Harlov et al., 2002, 2016; Jonsson et al., 2016). This interpretation is supported by monazite-xenotime thermometry (e.g., Heinrich et al., 1997; Pyle et al., 2001), which shows that the calculated temperatures for monazite-(Ce) inclusions in primary fluorapatite (630 ± 50 °C) are comparable to those obtained for primary monazite-(Ce) from the Olserum and Djupedal areas (averages of 540 to 640 °C) (Andersson et al., 2018a).

During subsequent cooling of the hydrothermal system and concurrent fracturing and recrystallisation of primary fluorapatite, monazite-(Ce) and xenotime-(Y) inclusions from the outer part of crystals (rims) and domains adjacent to fractures experienced dissolution. The dissolved REE and P were re-precipitated as new xenotime-(Y) and monazite-(Ce) present within the surrounding mineral groundmass and within fractures of the fluorapatite crystals, as grains along the rims of the large crystals, and in between recrystallised grains. This remobilisation event is recorded by the internal textural zoning in primary fluorapatite crystals as shown by compositional differences between crystal cores with inclusion-rich domains compared to inclusion-absent domains. The differences between these different domains are mostly small and only detectable on the scale of individual samples (Figs. FEA1, FEA2, and FEA3). They are much smaller than the first-order compositional variations of primary fluorapatite along the fluid flow path. We therefore interpret these secondary changes in the fluorapatite composition as the product of partial re-equilibration of primary fluorapatite with local fracture fluids rather than reflecting a major episode of an influx of new hydrothermal fluids.

Secondary fluorapatite formed by the partial to pervasive alteration of monazite-(Ce), which probably coincided with or partly preceded the late-stage remobilisation event. The normalised REE ratios (La/Yb, La/Sm, and Gd/Yb) of secondary fluorapatite show distinct trends, discriminating the secondary fluorapatite from primary fluorapatite (Fig. 6). The contrasting textural relations and chemical trends clearly demonstrate that secondary fluorapatite formed later than the primary fluorapatite. The REE distribution in secondary fluorapatite was probably controlled by the reaction with local fracture

fluids or growth competition with other co-crystallising replacement REE-bearing minerals rather than changes in primary fluid compositions. For instance, the higher $(La/Sm)_N$ and the lower $(Gd/Yb)_N$ ratios, compared to primary fluorapatite, indicate that secondary fluorapatite incorporated more LREE and HREE. This is consistent with the strong depletion in HREE found in pervasively altered monazite-(Ce) (Andersson et al., 2018a).

5.2. Apatite as a tracer of the source of ore-forming fluids

5.2.1. Stable Cl isotopic composition

The stable isotope (e.g., B, C, H, O, and S) composition of hydrothermal minerals has been commonly used for tracing the source and migration of ore-forming fluids (e.g., Ohmoto, 1972; Taylor, 1997; Seal, 2006; Slack and Trumbull, 2011; Downes et al., 2014; Broom-Fendley et al., 2016b). Chlorine is the most important complexing ligand in ore-forming fluids, including REE-mineralising systems along with F (e.g., Banks et al., 2000a, 2000b; Migdisov et al., 2009; 2016; Williams-Jones and Migdisov, 2014). In addition, because the Cl isotopic composition of the source is likely to be inherited by hydrothermal fluids (Selverstone and Sharp, 2015), identifying the source signature of Cl should hold a major potential to track down the ultimate source of ore metals and ore-forming fluids. The best approach would be to determine the Cl isotopic composition of ore-stage fluid inclusions (Banks et al., 2000a, 2000b; Chiaradia et al., 2006; Gleeson and Smith, 2009; Nahnybida et al., 2009). This, however, faces considerable challenges because in many hydrothermal ore deposits, the fluid inclusion record is incomplete or even obliterated, and post-entrapment modification may have affected the fluid inclusions. In addition, current analytical techniques only permit the analysis of $\delta^{37}Cl$ from bulk crush-leach samples, which in many cases results in averaging the composition of multiple generations of fluid inclusions. Direct determination of $\delta^{37}Cl$ for the fluid inclusions responsible for ore-formation is only possible in rare cases. Therefore, analysis of the Cl isotope composition of Cl-rich hydrothermal minerals has the potential to provide key information about the source of the fluids.

A key prerequisite for calculating the $\delta^{37}Cl$ value of the hydrothermal fluid from that of a mineral, which was in equilibrium with and precipitated from the same fluid, is knowledge of the temperature-

dependent fluid-mineral fractionation. Experimental data for Cl isotopic fractionation between apatite and aqueous fluids at hydrothermal temperatures are currently unavailable. However, *ab initio* and lattice dynamics modelling of mono- and divalent metal chloride systems (NaCl and KCl, and $FeCl_2$ and $MnCl_2$; Schauble et al., 2003) show that the heavier ^{37}Cl isotope favours the divalent species. The magnitude of this fractionation is about 2-3‰ at 25 °C and only 0.55-0.85‰ at 300 °C. The divalent chlorides can be considered analogues to minerals where Cl is bonded to divalent cations, such as biotite, amphibole, and apatite. Combining the modelling results with measured fractionation factors between monovalent chlorides and co-existing brines at 22-28 °C, which are on the order of 1.00026-1.00055 (or $\Delta_{NaCl\text{-}brine}$ of 0.26-0.55‰) and 0.99991-1.00025 (or $\Delta_{KCl\text{-}brine}$ of -0.09 to 0.25‰; Eggenkamp et al., 1995; Luo et al., 2014), apatite is expected to have a ~2-3‰ higher $\delta^{37}Cl$ value than the co-existing fluid at 25 °C. The fractionation factors between mono- and divalent chlorides strongly decrease with temperature and it can be assumed that fractionation between monovalent chlorides and co-existing brines will be very small at temperatures of 300 °C. Therefore, the Cl isotope fractionation factor between apatite and co-existing fluid is estimated to be about 1.0005-1.0010 (or $\Delta_{apatite\text{-}fluid}$ of 0.5-1.0‰). At even higher temperatures of 500-600 °C, fractionation is expected to be much smaller with the fractionation factor approaching unity. Preliminary experimental work indicates a fractionation factor between amphibole and a NaCl-rich fluid of 1.0002 (or $\Delta_{amphibole\text{-}fluid}$ of 0.19‰ ± 0.23‰) at 700 °C and 200 MPa (Cisneros, 2013).

The $\delta^{37}Cl$ values of primary fluorapatite from the Olserum-Djupedal REE-phosphate mineralisation range between -0.7 and +1.6‰ (Figs. 9 and 10). If we assume a small fractionation factor (1.0000-1.0005 or $\Delta_{apatite\text{-}fluid} < 0.5$‰) between fluorapatite and co-existing fluid at about 600 °C, the initial $\delta^{37}Cl$ value of the ore-forming fluid, as calculated from the data of granite-hosted fluorapatite, should be in the range of 1.1-1.6‰. Comparing this to potential fluid sources, hydrothermal fluids produced primarily by magmatic fluid exsolution or by metamorphic devolatilisation can have similar rather heavy isotopic compositions (Fig. 9). Magmatic fluids exhibit a large range in $\delta^{37}Cl$, from strikingly negative values in porphyry Cu environments to about +2.0‰ in fluids associated with the Sn-W mineralised Cornubian batholith in SW England (Fig. 9; Eastoe and Guilbert, 1992; Eggenkamp, 1994;

Musashi et al., 1998; Banks et al., 2000a, 2000b, Chiaradia et al., 2006; Gleeson and Smith, 2009; Nahnybida et al., 2009). Such a large variation probably reflects partial inheritance of the Cl isotopic signatures from the source rocks to the partial melts, host-rock contamination during emplacement of plutons, combined with isotopic fractionation due to fluid-rock interaction or degassing.

The primary ore-forming fluid in the Olserum-Djupedal REE-phosphate mineralisation is currently interpreted as magmatic, derived from the adjacent TIB granite (Anderson et al., 2018b). This granite is part of the anatectic-group granites in the Västervik region (Nolte et al., 2011, Kleinhanns et al., 2015) that have chemical affinities (ferroan, peraluminous, and calc-alkalic) and field relationships that suggest an origin by low-pressure melting of metasedimentary rocks in an extensional regime (cf. Frost and Frost, 2011; Nolte et al., 2011, Kleinhanns et al., 2015). A similar petrogenesis has been proposed for the peraluminous granites of the Cornubian batholith (Chappel and Hine, 2006; Simons et al., 2016). This batholith produced aqueous ore-forming fluids with a $\delta^{37}Cl$ range of 1.7 to 2.0‰ (Banks et al., 2000a, 2000b), which is similar to the initial $\delta^{37}Cl$ values of 1.1-1.6‰ calculated for the ore-forming fluid in Olserum-Djupedal. We therefore propose that the moderately positive $\delta^{37}Cl$ values of granite-hosted fluorapatite and the generally higher values found in primary fluorapatite from the Olserum area record the unmodified magmatic fluid source signature, which was possibly inherited from the metasedimentary rocks during partial melting. Primary fluids derived from a magmatic source having less metasedimentary contributions, such as those from porphyry-type Cu deposits or rare-metal deposits related to alkaline-peralkaline magmatic systems, are expected to have $\delta^{37}Cl$ values closer to mantle signatures (Fig. 9).

Because metamorphic dehydration reactions do not cause Cl isotopic fractionation (Selverstone and Sharp, 2015), fluids formed by devolatilisation inherit the $\delta^{37}Cl$ values from the source rocks, which will then range between about -3.6 to 2.2‰ (John et al., 2010; Selverstone and Sharp, 2013, 2015). Thus, a metamorphic fluid with a rather heavy isotopic signature could potentially also explain the high $\delta^{37}Cl$ values observed in fluorapatite from Olserum-Djupedal. However, involving an ultimately metamorphic fluid source would require a fluid flow system where fluids produced by devolatilisation would first flow towards the TIB granite, react with the granite, mobilise REE and P, and then flow out from the granite

into the metasedimentary host rocks. Such a fluid flow model would appear inconsistent with the current understanding of the fluid flow dynamics and hydrothermal evolution of granitoid intrusions. As demonstrated by physical fluid flow modelling, hot granitic intrusions impede colder external fluids to enter the crystallising intrusions, and only considerably cooled intrusions experience an inflow of cooler meteoric or other external fluids (Hanson, 1995; Weis, 2014, 2015).

5.2.2. Halogen ratios (Br/Cl and I/Cl)

The halogens, and particularly the Br/Cl and I/Cl ratios, are commonly utilised to trace sources of hydrothermal fluids, as variations in halogen concentrations and their ratios reflect processes such as seawater evaporation, precipitation and dissolution of halite, fluid mixing, interaction with organic-rich sedimentary rocks, fluid desiccation, and phase separation (e.g., Banks et al., 2000b; Svensen et al., 2001; Chiaradia et al., 2006; Kendrick et al., 2007; Gleeson et al., 2009; Seo et al., 2011; Kendrick and Burnard, 2013; Hammerli et al., 2014; Kusebauch et al., 2015a; Bernal et al., 2017; Fusswinkel et al., 2018). Using apatite as a proxy for the ore-forming fluids requires an understanding of the partitioning of the halogens between apatite and the co-existing fluid. Partitioning of Cl between apatite and fluid can potentially be dependent on many factors, including temperature, pressure, pH, and fluid composition (Kusebauch et al., 2015a, 2015b). For an apatite-fluid system, Kusebauch et al. (2015a, 2015b) stated that estimating the Cl concentration in the fluid using a partition coefficient is difficult because of too many unknown variables. Nevertheless, they reported a partition coefficient ($D^{Cl}_{apatite\text{-}fluid}$) of 2.3 based on the assumption that the apatite-fluid partitioning can, to a first approximation, be described by a lattice-strain model (Kusebauch et al., 2015b). For Br and I, only Kusebauch et al. (2015b) have determined partition coefficients between apatite and fluid experimentally ($D^{Br}_{apatite\text{-}fluid}$ and $D^{I}_{apatite\text{-}fluid}$). By fitting the data to a lattice-strain model, they report apatite-fluid partition coefficients of ~0.045 for Br and ~0.0025 for I, which indicate a rather significant fractionation of Br and I between apatite and co-existing fluid.

Using these partition coefficients and the average halogen concentrations of the earliest-formed apatite in the Olserum-Djupedal REE-phosphate mineralisation (granite-hosted fluorapatite; 840 ppm Cl, 1.1 ppm Br, and 0.76 ppm I; Table 2), results in apparent halogen concentrations of the primary ore-

560 forming fluid of 365 ppm Cl, 24.4 ppm Br, and 304 ppm I, corresponding to molar ratios $Br/Cl \cdot 10^{-3}$ of
561 ~30, $I/Cl \cdot 10^{-6}$ of ~232500, and Br/I of ~0.13. This estimated halogen composition is far away from any
562 known crustal fluid composition and would plot within the extension of the grey shaded field with molar
563 Br/I ratios of 0.05-0.4 in Figure 11. This field was constructed for a salinity range of 1-20 wt% NaCl
564 using the fitted and the experimentally-derived partition coefficients ($D^{Br}_{apatite\text{-}fluid}$ and $D^{I}_{apatite\text{-}fluid}$) given
565 for a NaCl-rich fluid at 500-700 °C and 200 MPa (Kusebauch et al., 2015b). This approach eliminates the
566 need to calculate the Cl concentration in the fluid from $D^{Cl}_{apatite\text{-}fluid}$ values. All compositions within this
567 field have molar I concentrations exceeding Br concentrations up to an order of magnitude, a feature
568 never observed in any crustal fluid and which cannot be explained by any known process or fluid source
569 halogen signature. We therefore consider these fluid compositions estimated from the partition
570 coefficients to be implausible. The inconsistency with the available experimental data may be related to
571 pH effects, or the influence of absolute Cl, Br, and I concentrations in the fluids on the partitioning
572 behaviour, an effect already noted by Kusebauch et al. (2015b).

573 The altered primary fluorapatite in the Olserum area has Br/Cl and I/Cl molar ratios distinctly
574 different from those of other primary fluorapatites. Its halogen ratios overlap with and plot on the same
575 Br/I ratio trend as those of Na-Ca and Ca-Na brine fluid inclusions analysed by LA-ICP-MS (Fig. 11;
576 Andersson, 2019). These fluid inclusions are interpreted to be related to the alteration of this fluorapatite.
577 The brine inclusions for which Br/Cl and I/Cl data could be obtained were trapped at around 300 °C and
578 sometimes contain hematite as a trapped solid phase, implying that hematite was stable during fluid
579 entrapment. Hematite extensively replaces magnetite in the surrounding mineral groundmass of the
580 altered fluorapatite (Fig. 2E). We therefore infer that the fluorapatite was altered by this fluid and
581 inherited its halogen signature, while the surrounding magnetite was concomitantly altered to hematite.
582 The high Sr and Pb concentrations measured in the fluid inclusions (Andersson, 2019) are also consistent
583 with the anomalously high Sr and, in part, Pb contents of this fluorapatite (Table 2) as these elements
584 strongly partition into apatite (Pan and Fleet, 2002). This apatite-fluid pair does not indicate an order of
585 magnitude fractionation between Br and I. In fact, Br/I ratios are relatively similar for fluorapatite and the

586 co-existing fluid (Fig. 11). If we calculate $D^{Br}_{apatite\text{-}fluid}$ values for this apatite-fluid pair, they range from
587 0.003 to 0.009, which agrees relatively well with previous experimental data (Kusebauch et al., 2015b).
588 The difference lies solely in the $D^{I}_{apatite\text{-}fluid}$ values and calculated values for this apatite-fluid pair range
589 from 0.006 to 0.013x.

590 This lower-temperature apatite-fluid pair indicates only a minor fractionation of Br from I during
591 apatite precipitation, with $D_{apatite\text{-}fluid}$ values far less than an order of magnitude apart. Assuming this to be
592 the case at higher temperatures, the fluid that formed the granite-hosted fluorapatite would have Br/Cl and
593 I/Cl ratios close to those of this fluorapatite (Fig. 11). Such a fluid halogen composition would be quite
594 plausible for magmatic-hydrothermal fluids, being very close to the field defined by magmatic fluids from
595 S-type granites of the Cornubian batholith (Fig. 11; Böhlke and Irwin, 1992; Irwin and Roedder, 1995;
596 Banks et al., 2000a, 2000b). The Br/Cl ratios do also overlap with those of magmatic fluids from the Sn-
597 W mineralised Mole granite in Australia (molar $Br/Cl \cdot 10^{-3}$ values of 0.84-0.92; Seo et al., 2011). The
598 slightly elevated I/Cl ratios of the granite-hosted fluorapatite could potentially reflect a source of the
599 granitic melts that was relatively enriched in I compared to the granites from the Cornubian batholith. The
600 above interpretation must be treated with some caution because it is based on the assumption of only a
601 very small Br-I fractionation during apatite precipitation from high-temperature hydrothermal fluids,
602 similar to what we have observed for the lower-temperature apatite-fluid pair. Nevertheless, halogen
603 ratios of the primary hydrothermal fluid similar to that of the granite-hosted fluorapatite are plausible for
604 a magmatic-hydrothermal fluid related to S-type magmatism and are in line with our other findings.

605 Other potential fluid sources include metamorphic fluids, or formation waters; the latter being
606 either residual bittern brines, which attain high Br/Cl and slightly elevated I/Cl ratios due to evaporation
607 of seawater, or halite dissolution brines acquiring low Br/Cl and I/Cl ratios (Fig. 11; e.g., Kendrick and
608 Burnard, 2013; Fusswinkel et al., 2018). However, the involvement of formation waters can be ruled out
609 because of the distinctly different halogen ratios of the granite-hosted fluorapatite. The halogen signatures
610 of metamorphic fluids vary, but they tend to have Br/Cl ratios close to mantle or primitive magmatic
611 values, and can extend to much higher values and elevated I/Cl ratios reflecting interaction with organic-

matter rich lithologies (Svensen et al., 2001; Kendrick and Burnard, 2013; Miron et al., 2013; Rauchenstein-Martinek et al. 2016; Fusswinkel et al., 2018). The halogen data of the primary fluorapatite from the Olserum-Djupedal REE-phosphate mineralisation would be compositionally compatible with metamorphic fluids. However, a metamorphic formation model would disagree with constraints placed by the fluid flow dynamics of granitoid intrusions as discussed above.

5.3. Apatite as a tracer of the chemistry and evolution of ore-forming fluids

5.3.1. Halogen composition of ore-forming fluids

Our complete halogen data of apatite make it possible to estimate the halogen composition of the ore-forming fluids. If fluorapatite is the dominant end-member and the Cl content is rather high, both F and Cl must clearly be important constituents of the fluid. Using standard state thermodynamic properties for F-, Cl- and OH-apatite end-members (Tacker and Stormer; 1989; Zhu and Sverjensky, 1991), the activity ratios ($\alpha_{HCl}/\alpha_{H2O}$) or fugacity ratios ($f_{HCl}/f_{H2O}$) of the co-existing fluid can be estimated. As a first-order approximation, this calculation can be performed assuming an ideal mixing model for OH, F, and Cl on the X-site in apatite (e.g., Boudreau et al., 1993; Piccoli and Candela, 1994, 2002; Treloar and Colley, 1996, Rasmussen and Mortensen, 2013; Webster and Piccoli, 2015), although recent studies suggest a moderate non-ideal mixing on the F-Cl apatite and F-OH apatite joins (Hovis and Harlov, 2010; Hovis et al., 2014). Yet, these effects are smaller than the uncertainty on the standard state thermodynamic properties. We have thus calculated the values of $\log(f_{H2O}/f_{HCl})$, $\log(f_{H2O}/f_{HF})$, and $\log(f_{HF}/f_{HCl})$ for the ore-forming fluid in equilibrium with primary fluorapatite at 600-650 °C and 200 MPa using the HCh software package (Shvarov, 2008) using the following exchange reactions:

$$Ca_5(PO_4)_3OH + HCl(g) = Ca_5(PO_4)_3Cl + H_2O(g) \quad (3)$$

$$Ca_5(PO_4)_3OH + HF(g) = Ca_5(PO_4)_3F + H_2O(g) \quad (4)$$

$$Ca_5(PO_4)_3F + HCl(g) = Ca_5(PO_4)_3Cl + HF(g) \quad (5)$$

Thermodynamic data for apatite end-members were adopted from Zhu and Sverjensky (1991), and those for HCl(g), HF(g), and $H_2O(g)$ from Frenkel et al. (1994). The values of $\log(f_{H2O}/f_{HCl})$, $\log(f_{H2O}/f_{HF})$, and $\log(f_{HF}/f_{HCl})$ correlate well with values calculated for biotite (Fig. 12). In general, this indicates that the

granite-derived fluid responsible for the primary REE mineralisation was dominantly Cl-rich but with a significant F component. The F component then gradually decreased towards the metasediment-hosted REE ore in the Olserum area and subsequently to the Bersummen and Djupedal areas.

This observation has direct implications for the transport behaviour of REE and high field strength elements (HFSE) such as Th and Nb. Experiments have shown that both Th and Nb are more soluble in aqueous fluids containing high concentrations of F because of the formation of stable metal-fluoride species (Keppler and Wyllie, 1990, 1991; Timofeev et al., 2015). The REE are mobile in Cl-bearing fluids, both with and without F (e.g., Migdisov et al., 2009, 2016). Because of the strong partitioning of F into apatite, F loss to apatite would potentially lead to the destabilisation of the HFSE and REE fluoride complexes, promoting precipitation of HFSE-bearing minerals early in the paragenetic sequence. This would explain why rare primary (REE,Y,Th,U,Ca)-(Nb,Ta)-oxides occur only in the Olserum area but not in the Djupedal and Bersummen areas (Andersson et al., 2018a).

5.3.2. Trace elements in apatite and their significance for the chemistry and evolution of ore-forming fluids

The trace element composition of apatite, particularly the Mg, Mn, Pb, REE, Sr, Th, U, V, and Y contents, can discriminate between different mineralisation styles and host-rock affinities (Belousova et al., 2002; Mao et al., 2016). Apatite associated with carbonatites is usually very LREE-rich and contains high Sr concentrations, whereas apatite forming in granitic environments shows less fractionation between LREE and HREE, displays clear Eu anomalies, and typically has lower Sr and higher Mn contents (Belousova et al., 2002; Mao et al., 2016; Chakhmouradian et al., 2017). These characteristic features of granite-associated apatite are also evident in the fluorapatite data of the Olserum-Djupedal REE-phosphate mineralisation (Figs. 5 and 7).

Several studies have shown that combined textural and mineral-chemical data on (REE+Y) in apatite are particularly suitable for identifying metasomatic overprinting or alteration of apatite. This is manifested by domains in apatite depleted in (REE+Y) frequently combined with the presence of abundant monazite or xenotime inclusions (e.g., Harlov et al., 2002, 2005; Harlov and Förster, 2003;

Harlov, 2015; Jonsson et al., 2016; Krneta et al., 2016). For the fluorapatite from the Olserum-Djupedal REE-phosphate mineralisation, the compositional data on (REE+Y) reveals several interesting features that can be interpreted in terms of the chemistry and evolution of the ore-forming fluid.

The normalised La/Yb, La/Sm, and Gd/Yb ratios of primary fluorapatite show distinct trends that track the deposit-scale compositional zoning pattern. They further discriminate the primary from the secondary fluorapatite (Figs. 6, 8B, and 10B). Therefore, the REE ratios of the primary fluorapatite should reflect the evolution of the fluid and the partitioning of REE among fluorapatite and co-crystallising monazite-(Ce) and xenotime-(Y). It is, however, difficult to assess whether the measured REE ratios fully reflect those of the initial fluid or if they were partly modified by the subsequent autometasomatism. This is because the primary fluorapatite lacks domains that are clearly unaltered and could yield the original (REE+Y) composition. Nevertheless, fluorapatite co-crystallising with monazite-(Ce) and xenotime-(Y) should yield REE distribution patterns with pronounced enrichment in the MREE because of the strong partitioning of the REE in the range Nd-Gd into fluorapatite (Fleet and Pan, 1995, 1997). The Olserum-Djupedal samples show exactly such patterns (Fig. 5). The change in REE ratios in the sequence from the granite-hosted to the metasediment-hosted mineralisations in the Bersummen and Djupedal areas thus either reflect increasing co-crystallisation of monazite-(Ce) over xenotime-(Y), or increasing nucleation of inclusions of monazite-(Ce) relative to xenotime-(Y).

For F-bearing fluids, solubility experiments show that the REE and Y are complexed differently with fluoride, where the REE form mono-fluoride ($REEF^{2+}$) and Y forms di-fluoride (YF_2^+) complexes at otherwise identical conditions (Migdisov et al., 2009; Loges et al., 2013). Because Y and Ho have nearly the same ionic radii and are both trivalent, they should be incorporated into apatite coherently during the precipitation from an aqueous fluid. However, if the fluids are F-rich, decoupling of Y from Ho is commonly observed and can occur because the high activity of F stabilises YF_2^+ over HoF^{2+} (Loges et al., 2013). Based on this interpretation of the experimental data, it can be predicted that primary granite-hosted fluorapatite from the Olserum-Djupedal REE-phosphate mineralisation, which formed from the most F-rich fluid in the hydrothermal system, should show the highest $(Y/Ho)_N$ ratios. This is indeed the

690 case and the $(Y/Ho)_N$ ratios decrease from 1.0 in the granite-hosted fluorapatite to 0.8 in primary
691 fluorapatite from the Bersummen area (Fig. 13). We thus infer that the $(Y/Ho)_N$ ratios in primary
692 fluorapatite from the Olserum-Djupedal REE-phosphate mineralisation clearly support our conclusions
693 about F-Cl fractionation and that the other normalised REE ratios also reflect features of the evolving
694 primary ore-forming fluid. The increase in $(Y/Ho)_N$ of primary fluorapatite from the Bersummen area to
695 the Djupedal area potentially reflects the reduced ability of F to control the uptake of Ho and Y at the
696 lower F activity in the Djupedal area, leading to a stronger control by co-crystallising REE minerals. The
697 absolute values of $(Y/Ho)_N$ are most likely also affected by Y-Ho partitioning involving the other REE-
698 bearing minerals, but the overall decrease is nevertheless significant. For secondary fluorapatite, which
699 generally has higher $(Y/Ho)_N$ ratios than the primary fluorapatite, inheritance from monazite-(Ce) and
700 growth competition with other replacement products probably exert the key control on the Y-Ho
701 incorporation.

702 For the other trace elements analysed, no clear relationship between the compositional changes
703 along the gradient from the proximal granite- to most distal metasediment-hosted primary fluorapatite,
704 can be observed. We therefore conclude that the concentrations of the other trace elements in fluorapatite
705 mostly reflect the local crystallisation environments, partitioning with co-crystallising minerals and host
706 rock interaction. More local control is also demonstrated by the internal textural zoning in the primary
707 fluorapatite where the concentrations of most trace elements analysed show distinct variations between
708 inclusion-rich and inclusion-absent domains. The consistent and relatively high Fe concentration (600-
709 5000 ppm; Table 2) in fluorapatite, comparable to apatite from magmatic-hydrothermal porphyry Cu
710 deposits (Mao et al., 2016), likely reflects high Fe concentrations in the primary ore-forming fluid, which
711 is rather typical for magmatic-hydrothermal systems (e.g., Campbell et al., 1995; Audédat et al., 2000;
712 Ulrich et al., 2002; Rusk et al., 2004).

713 *5.3.3. Evolving stable Cl isotopic compositions*

714 The Cl isotopic composition of the primary fluorapatite from the Olserum-Djupedal REE-
715 phosphate mineralisation shows a distinct trend of decreasing $\delta^{37}Cl$ values from about +1.6 to -0.7‰ in

716 the sequence from the proximal granite-hosted to the most distal metasediment-hosted samples (Figs. 9
717 and 10). Because the fractionation between co-existing apatite and fluid should be very small at
718 temperatures of 600 °C, we interpret the isotopic variation as a primary feature of a chemically evolving
719 fluid system. However, it is still possible that fractionation between the fluid and several co-existing Cl-
720 bearing minerals (fluorapatite, biotite, and gedrite) can produce such a change in the isotopic composition
721 of the fluorapatite. Kusebauch et al. (2015a, 2015c) suggested that the equilibrium fractionation between
722 a fluid and variably altered gabbro containing amphibole, scapolite, and apatite could explain a decrease
723 in $\delta^{37}Cl$ values from +1.0 to -0.5‰ if a bulk rock fractionation factor of about 1.0010 (or $\Delta_{\text{bulk rock-fluid}}$ =
724 +1.0‰) at 600 °C was assumed. An even higher fractionation factor of 1.0019 (or $\Delta_{\text{scapolite-fluid}} = +1.9‰$)
725 between scapolite and co-existing saline fluid above 500 °C was proposed to explain some very negative
726 $\delta^{37}Cl$ values in the ore-forming fluids of an IOCG system in Norrbotten, Sweden (Bernal et al., 2017).
727 The trend in decreasing $\delta^{37}Cl$ values for the Olserum-Djupedal REE-phosphate mineralisation can
728 be modelled by simple Rayleigh isotopic fractionation using the equation (Faure, 1986):
729 $$\delta^{37}Cl_{fluid} = [(\delta^{37}Cl^{0}_{fluid} + 1000)F^{\alpha-1}] - 1000 \quad (6)$$
730 where $\delta^{37}Cl_{fluid}$ and $\delta^{37}Cl^{0}_{fluid}$ are the final and initial $\delta^{37}Cl$ values of the fluid, respectively, α is
731 the fractionation factor between the co-existing fluid and the mineral(s) at a given temperature, and F is
732 the fraction of the fluid remaining (Faure, 1986; Kusebauch et al., 2015c). Assuming an initial $\delta^{37}Cl^{0}_{fluid}$
733 value of 1.4‰ (note that the $\delta^{37}Cl$ value of the initial fluid has no effect on the direction and magnitude of
734 the fractionation), only a bulk fractionation factor higher than 1.0005 can produce the observed variation
735 of about 2‰ (Fig. 14). This would require that over 95% ($F < 0.05$) of the original Cl, dissolved in the
736 fluid, would need to be consumed by mineral precipitation along the fluid flow path. If the fractionation
737 factor were as high as 1.0019, the same effect can be achieved when only 65% of the original Cl were
738 consumed. Alternatively, if we only consider the average $\delta^{37}Cl$ values of each fluorapatite-bearing
739 mineralisation, a decrease of 1.5‰ (down from +1.0‰ for granite-hosted to -0.5‰ for primary
740 fluorapatite in the Bersummen and Djupedal areas) would be achieved for 50% or 75% consumption of
741 the original Cl for fractionation factors of 1.0019 and 1.0010, respectively (Fig. 14).

742 This calculation demonstrates that if Rayleigh fractionation alone is responsible for the decrease in
743 $\delta^{37}Cl$, then either the fractionation factors between the minerals and co-existing fluid needs to be
744 significantly higher than currently estimated, or fluid-rock interaction needs to consume a significant and
745 somewhat unrealistic proportion of the Cl in the original fluid. An alternative process that can produce
746 this trend or add to the magnitude of fractionation given by the Rayleigh effect is kinetic fractionation
747 caused by differences in diffusion coefficients between the ^{35}Cl and ^{37}Cl isotopes (cf. Kusebauch et al.,
748 2015c; Barnes and Sharp, 2017). However, in advection-dominated fluid regimes, such as in magmatic-
749 hydrothermal environments, or in ore-forming settings in general, mass transport over large distances by
750 diffusion is probably insignificant compared to advective transport (e.g., Hobbs, 1987; Jamtveit and
751 Yardley, 1997; Heinrich and Candela, 2014; Weis, 2014, 2015). Thus, diffusion-controlled fractionation
752 should play a negligible role in the production of the deposit-scale Cl isotopic zoning pattern.
753 Another process that can potentially explain the trend of decreasing $\delta^{37}Cl$ is mixing of the primary
754 magmatic fluid with a second fluid having negative $\delta^{37}Cl$ values. Such a fluid could originate from
755 sedimentary pore fluids, which can attain very light Cl isotopic compositions due to interaction with
756 organic matter (Fig. 9; Barnes and Sharp, 2017). Additionally, metamorphic devolatilisation can also
757 produce fluids with negative $\delta^{37}Cl$ values depending on the Cl isotopic signature of the source rocks,
758 possibly affected by interaction with organic matter (Selverstone and Sharp, 2015). Considering the
759 distinct magmatic-hydrothermal ore-forming environment, a scenario involving mixing of a primary
760 magmatic fluid with a metamorphic fluid is certainly possible and could well explain the compositional
761 features of the primary fluorapatite from the Olserum-Djupedal REE-phosphate mineralisation.

762 ## 6. Conclusions

763 1) Combined *in situ* SIMS, EPMA, and LA-ICP-MS data of hydrothermal apatite from the Olserum-
764 Djupedal REE-phosphate mineralisation demonstrate that apatite has the capacity to preserve the
765 stable Cl isotope, halogen, and trace element signature inherited from the original ore-forming
766 fluid despite later overprinting fluid events.

2) The data from the primary ore-stage apatite show systematic changes in the halogen and Cl isotopic compositions along a flow path from the proximal granite-hosted to the most distal metasediment-hosted REE mineralisation. Tracing the ultimate source of the ore-forming fluid in such a system necessitates identifying the apatite with the chemically least evolved character.
3) The trace element composition in apatite generally reflects compositional features inherited from the host rocks rather than features of the ore-forming fluid, and the effects from growth competition with co-crystallising minerals. Only a few trace elements, notably the REE ratios, record the chemical characteristics of the ore-forming fluids.
4) The small fractionation of Br from I between apatite and fluid inclusions during the later stages of the Olserum-Djupedal REE hydrothermal system suggests that Br and I do not necessarily fractionate to the extent proposed earlier. The halogen compositions of apatite can thus be used as a first approximation for that of the ore-forming fluid. Because the partitioning of Cl between apatite and the fluid is not only dependent on the fluid composition, Br/Cl and I/Cl ratios of the ore-forming fluid can only be determined if fluid salinity can be measured or estimated. Together with the presumed small fractionation factors for Cl isotopes between apatite and co-existing fluid at high temperatures, the stable Cl isotopic composition and halogen compositions of apatite can jointly be used to trace the source of ore-forming fluids.

Acknowledgements

This study was supported by a grant to SSA from the GeoDoc Graduate Programme (Graduate School, Faculty of Sciences, University of Helsinki) and supplementary funding from the Academy of Finland (Project No. 280458) to TW. EJ acknowledges the support of SGU. We thank Tasman Metals and Leading Edge Materials for support during fieldwork and for granting access to proprietary information. The staff of the SGU national drillcore archive in Malå is thanked for their kind support during logging and sampling of drill cores. We thank Lev Ilyinsky and Kerstin Lindén (NORDSIM facility, Sweden) for their valuable help during the SIMS analysis, Helena Korkka for the preparation of thick sections used in this study, and Radoslaw Michallik for assistance with electron-probe microanalysis. Dan Harlov (GFZ Potsdam, Germany) is warmly thanked for donating synthetic REE- and Y-phosphate and chlor- and fluorapatite reference materials. We would like to thank Dan Harlov, Cyril Chelle-Michou and one anonymous reviewer for their useful comments and suggestions. The NORDSIM facility operates as a Swedish national infrastructure supported by Vetenskapsrådet. This is NORDSIM contribution #602.

References

Andersen, T., Andersson, U. B., Graham, S., Åberg, G. and Simonsen, S. L. (2009) Granitic magmatism by melting of juvenile continental crust: new constraints on the source of Palaeoproterozoic granitoids in Fennoscandia from Hf isotopes in zircon. *J. Geol. Soc. London* **166**, 233–247.

Andersson, S. S., Wagner, T., Jonsson, E. and Michallik, R. M. (2018a) Mineralogy, paragenesis and mineral chemistry of REE's in the Olserum-Djupedal REE-phosphate mineralization, SE Sweden. *Am. Mineral.* **103**, 125–142.

Andersson, S. S., Wagner, T. Jonsson, E., Fusswinkel, T., Leijd, M. and Berg, J. T. (2018b) Origin of the high-temperature Olserum-Djupedal REE-phosphate mineralisation, SE Sweden: a unique contact metamorphic-hydrothermal system. *Ore Geol. Rev.* **101**, 740–764.

Andersson, S. S. (2019) Formation of hydrothermal REE-phosphate deposits. PhD thesis, University of Helsinki.

Arcuri, T. and Brimhall, G. (2003). The chloride source for atacamite mineralization at the Radomiro Tomic porphyry copper deposit, northern Chile. *Econ. Geol.* **98**, 1667–1681.

Audétat, A., Güther, D. and Heinrich, C. A. (2000) Causes for large-scale metal zonation around mineralized plutons: fluid inclusion LA-ICP-MS evidence from the Mole granite, Australia. *Econ. Geol.* **95**, 1563–1581.

Banks, D. A., Gleeson, S. A. and Green, R. (2000a) Determination of the origin of salinity in granite-related fluids: evidence from chlorine isotopes in fluid inclusions. *J. Geochem. Explor.* **69-70**, 309–312.

Banks, D. A., Green, R., Cliff, R. A. and Yardley, B. W. D. (2000b) Chlorine isotopes in fluid inclusions: determination of the origins of salinity in magmatic fluids. *Geochim. Cosmochim. Acta* **64**, 1785–1789.

Barnes, J. D. and Sharp, Z. D. (2017) Chlorine Isotope Geochemistry. *Rev. Mineral. Geochemistry* **82**, 345–378.

Barnes, J. D., Sharp, Z. D. and Fischer, T. P. (2008) Chlorine isotope variations across the Izu-Bonin-Mariana arc. *Geology* **36**, 883–886.

Barnes, J. D., Sharp, Z. D., Fischer, T. P., Hilton, D. R. and Carr, M. J. (2009) Chlorine isotope variations along the Central American volcanic front and back arc. *Geochemistry, Geophys. Geosystems* **10**. 1–17.

Bellucci, J. J., Whitehouse, M. J., John, T., Nemchin, A. A., Snape, J. F., Bland, P. A. and Benedix, G. K. (2017) Halogen and Cl isotopic systematics in Martian phosphates: implications for the Cl cycle and surface halogen reservoirs on Mars. *Earth Planet. Sci. Lett.* **458**, 192–202.

Belousova, E. A., Griffin, W. L., O'Reilly, S. Y. and Fisher, N. I. (2002) Apatite as an indicator mineral for mineral exploration: trace-element compositions and their relationship to host rock type. *J. Geochemical Explor.* **76**, 45–69.

Bernal, N. F., Gleeson, S. A., Smith, M. P., Barnes, J. D., Pan, Y. and Barnes, J. D. (2017) Evidence of multiple halogen sources in scapolites from iron oxide-copper-gold (IOCG) deposits and regional Na–Cl metasomatic alteration, Norrbotten County, Sweden. *Chem. Geol.* **451**, 90–103.

Beunk, F. F. and Page, L. M. (2001) Structural evolution of the accretional continental margin of the Paleoproterozoic Svecofennian orogen in southern Sweden. *Tectonophysics* **339**, 67–92.

Böhlke, J. K. and Irwin, J. J. (1992) Laser microprobe analyses of Cl, Br, I, and K in fluid inclusions: implications for sources of salinity in some ancient hydrothermal fluids. *Geochim. Cosmochim. Acta* **56**, 203–225.

Boudreau, A. E. and McCallum, I. S. (1989). Investigations of the Stillwater Complex: Part V. apatites as indicators of evolving fluid composition. *Contrib. to Mineral. Petrol.* **102**, 138–153.

Boudreau, A. E., Love, C. and Hoatson, D. M. (1993) Variation in the composition of apatite in the Munni Munni Complex and associated intrusions of the West Pilbara Block, Western Australia. *Geochim. Cosmochim. Acta* **57**, 4467–4477.

Broom-Fendley, S., Styles, M. T., Appleton, J. D., Gunn, G. and Wall, F. (2016a) Evidence for dissolution-reprecipitation of apatite and preferential LREE mobility in carbonatite-derived late-stage hydrothermal processes. *Am. Mineral.* **101**, 596–611.

Broom-Fendley, S., Heaton, T., Wall, F. and Gunn, G. (2016b) Tracing the fluid source of heavy REE mineralisation in carbonatites using a novel method of oxygen-isotope analysis in apatite: the example of Songwe Hill, Malawi. *Chem. Geol.* **440**, 275–287.

Campbell, L. S. and Henderson, P. (1997) Apatite paragenesis in the Bayan Obo REE-Nb-Fe ore deposit, Inner Mongolia, China. *Lithos* **42**, 89–103.

Campbell, A. R., Banks, D. A., Phillips, R. S. and Yardley, B. W. D. (1995) Geochemistry of Th-U-REE mineralizing magmatic fluids, Capitan Mountains, New Mexico. *Econ. Geol.* **90**, 1271–1287.

Chakhmouradian, A. R., Reguir, E. P., Zaitsev, A. N., Couëslan, C., Xu, C., Kynický, J., Mumin, A. H. and Yang, P. (2017) Apatite in carbonatitic rocks: compositional variation, zoning, element partitioning and petrogenetic significance. *Lithos* **274–275**, 188–213.

Chappell, B. W. and Hine, R. (2006) The Cornubian Batholith: an example of magmatic fractionation on a crustal scale. *Resour. Geol.* **56**, 203–244.

Chew, D. M., Babechuk, M. G., Cogné, N., Mark, C., O'Sullivan, G. J., Henrichs, I. A., Doepke, D. and McKenna, C. A. (2016) (LA,Q)-ICPMS trace-element analyses of Durango and McClure Mountain apatite and implications for making natural LA-ICPMS mineral standards. *Chem. Geol.* **435**, 35–48.

Chiaradia, M., Banks, D., Cliff, R., Marschik, R. and Haller, A. (2006) Origin of fluids in iron oxide-copper-gold deposits: constraints from $\delta^{37}Cl$, $^{87}Sr/^{86}Sr$ and Cl/Br. *Miner. Depos.* **41**, 565–573.

Cisneros, M. (2013) An experimental calibration of chlorine isotope fractionation between amphibole and fluid at 700 °C and 0.2 GPa. M.Sc. thesis, University of Texas.

Doherty, A. L., Webster, J. D., Goldoff, B. A. and Piccoli, P. M. (2014) Partitioning behavior of chlorine and fluorine in felsic melt-fluid(s)-apatite systems at 50MPa and 850-950 °C. *Chem. Geol.* **384**, 94–109.

Downes, P. J., Demény, A., Czuppon, G., Jaques, A. L., Verrall, M., Sweetapple, M., Adams, D., McNaughton, N. J., Gwalani, L. G. and Griffin, B. J. (2014) Stable H–C–O isotope and trace element geochemistry of the Cummins Range Carbonatite Complex, Kimberley region, Western Australia: implications for hydrothermal REE mineralization, carbonatite evolution and mantle source regions. *Miner. Depos.* **49**, 905–932.

Eastoe, C. J. and Guilbert, J. M. (1992) Stable chlorine isotopes in hydrothermal processes. *Geochim. Cosmochim. Acta* **56**, 4247–4255.

Eastoe, C. J., Long, A. and Knauth, L. P. (1999) Stable chlorine isotopes in the Palo Duro Basin, Texas: evidence for preservation of Permian evaporite brines. *Geochim. Cosmochim. Acta.* **63**, 1375–1382.

Eastoe, C. J., Long, A., Land, L. S. and Kyle, J. R. (2001) Stable chlorine isotopes in halite and brine from the gulf coast basin: brine genesis and evolution. *Chem. Geol.* **176**, 343–360.

Eastoe, C. J., Peryt, T. M., Petrychenko, O. Y. and Geisler-Cussey, D. (2007) Stable chlorine isotopes in Phanerozoic evaporites. *Appl. Geochemistry* **22**, 575–588.

Eggenkamp, H. G. M. (1994) $\delta^{37}Cl$: The geochemistry of chlorine isotopes. PhD thesis, Universiteit Utrecht.

Eggenkamp, H. G. M., Kreulen, R. and Koster Van Groos, A. F. (1995) Chlorine stable isotope fractionation in evaporites. *Geochim. Cosmochim. Acta* **59**, 5169–5175.

Faure, G. (1986) Principles of isotope geology. Second ed. John Wiley & Sons, New York.

Fleet, M. E. and Pan, Y. (1995) Crystal chemistry of rare earth elements in fluorapatite and some calc-silicates. *Eur. J. Mineral.* **7**, 591–605.

Fleet, M. E. and Pan, Y. (1997) Rare earth elements in apatite: uptake from H_2O-bearing phosphate-fluoride melts and the role of volatile components. *Geochim. Cosmochim. Acta* **61**, 4745–4760.

Frenkel, M., Kabo, G. J., Marsh, K. N., Roganov, G. N. and Wilhoit, R. C. (1994) Thermodynamics of organic compounds in the gas state, Vol 1. TRC Press, Texas.

Frietsch, R. and Perdahl, J. A. (1995) Rare earth elements in apatite and magnetite in Kiruna-type iron ores and some other iron ore types. *Ore Geol. Rev.* **9**, 489–510.

Frost, C. D. and Frost, B. R (2011) On ferroan (A-type) granitoids: their compositional variability and modes of origin. *J. Petrol.* **52**, 39–53.

Fullerton, W. (2014) REE mineralisation and metasomatic alteration in the Olserum metasediments. M.Sc. thesis, Lund University.

Fusswinkel, T., Giehl, C., Beermann, O., Fredriksson, J. R., Garbe-Schönberg, D., Scholten, L. and Wagner, T. (2018) Combined LA-ICP-MS microanalysis of iodine, bromine and chlorine in fluid inclusions. *J. Anal. At. Spectrom.* **33**, 768–783.

Gaal, G. and Gorbatschev, R. (1987) An outline of the Precambrian evolution of the Baltic Shield. *Precambrian Res. Elsevier Sci. Publ. B.V* **35**, 15–52.

Gavelin, S. (1984) The Västervik area in south-eastern Sweden. Studies in Proterozoic sedimentation, high-grade metamorphism and granitization. *Geological Survey of Sweden **Ba 32***, 172 pp.

Gleeson, S. A. and Smith, M. P. (2009) The sources and evolution of mineralising fluids in iron oxide-copper-gold systems, Norrbotten, Sweden: constraints from Br/Cl ratios and stable Cl isotopes of fluid inclusion leachates. *Geochim. Cosmochim. Acta* **73**, 5658–5672.

Goldoff, B., Webster, J. D. and Harlov, D. E. (2012) Characterization of fluor-chlorapatites by electron probe microanalysis with a focus on time-dependent intensity variation of halogens. *Am. Mineral.* **97**, 1103–1115.

Gorbatschev, R. (2004) The Transscandinavian Igneous Belt – Introduction and background. *Geol. S. Finl.* **37**, 9-15.

Guillong, M., Meier, D. L., Allan, M. M., Heinrich, C. A. and Yardley, B. W. D. (2008) SILLS: a MATLAB-based program for the reduction of laser ablation ICP-MS data of homogeneous materials and inclusions. *Mineralogical Association of Canada Short Course Volumes* **40**, 328–333.

Hammerli, J., Spandler, C., Oliver, N. H. S. and Rusk, B. (2014) Cl/Br of scapolite as a fluid tracer in the earth's crust: insights into fluid sources in the Mary Kathleen Fold Belt, Mt. Isa Inlier, Australia. *J. Metamorph. Geol.* **32**, 93–112.

Hansen, E. C. and Harlov, D. E. (2007) Whole-rock, phosphate, and silicate compositional trends across an amphibolite- to granulite-facies transition, Tamil Nadu, India. *J. Petrol.* **48**, 1641–1680.

Hanson, R. B. (1995) The hydrodynamics of contact metamorphism. *Geol. Soc. Am. Bull.* **107**, 595–611.

Harlov, D. E. (2015) Apatite: a fingerprint for metasomatic processes. *Elements* **11**, 171–176.

Harlov, D. E. and Förster, H.-J. (2002) High-grade fluid metasomatism on both a local and a regional scale: the Seward Peninsula, Alaska, and the Val Strona di Omegna, Ivrea-Verbano zone, Northern Italy. Part I: petrography and silicate mineral chemistry. *J. Petrol.* **43**, 801–824.

Harlov, D. E. and Förster, H.-J. (2003) Fluid-induced nucleation of (Y+REE)-phosphate minerals within apatite: nature and experiment. Part II. Fluorapatite. *Am. Mineral.* **88**, 1209–1229.

Harlov, D. E., Andersson, U. B., Förster, H.-J., Nystrom, J. O., Dulski, P. and Broman, C. (2002) Apatite–monazite relations in the Kiirunavaara magnetite–apatite ore, northern Sweden. *Chem. Geol.* **191**, 47–72.

Harlov, D. E., Wirth, R. and Förster, H.-J. (2005) An experimental study of dissolution – reprecipitation in fluorapatite: fluid infiltration and the formation of monazite. *Contrib. to Mineral. Petrol.* **150**, 268–286.

Harlov, D. E., Meighan, C. J., Kerr, I. D. and Samson, I. M. (2016) Mineralogy, chemistry, and fluid-aided evolution of the Pea Ridge Fe oxide-(Y + REE) deposit, Southeast Missouri, USA. *Econ. Geol.* **111**, 1963–1984.

Heinrich, C. A. and Candela, P. A. (2014) Fluids and ore formation in the Earth's crust. In *Treatise on Geochemistry, 2nd edition* (eds. H. D. Holland and K. K. Turekian), Elsevier Ltd., Oxford, pp. 1–28.

Heinrich, W., Andrehs, G. and Franz, G. (1997) Monazite-xenotime miscibility gap thermometry. I. An empirical calibration. *J. Metamorph. Geol.* **15**, 3–16.

Hobbs, B. E. (1987) Principles involving mobilization and remobilization. *Ore Geol. Rev.* **3**, 37–45.

Hoeve, J. (1974) Soda metasomatism and radio-active mineralisation in the Västervik area, southeastern Sweden. PhD thesis, Vrije University.

Hoeve, J. (1978) Composition and volume changes accompanying soda metasomatic alterations, Västervik area, SE Sweden. *Geol. Rundsch.* **67**, 920–942.

Hovis, G. L. and Harlov, D. E. (2010) Solution calorimetric investigation of fluor-chlorapatite crystalline solutions. *Am. Mineral.* **95**, 946–952.

Hovis, G. L., McCubbin, F. M., Nekvasil, H., Ustunisik, G., Woerner, W. R. and Lindsley, D. H. (2014) A novel technique for fluorapatite synthesis and the thermodynamic mixing behavior of F-OH apatite crystalline solutions. *Am. Mineral.* **99**, 890–897.

Hughes, J. M. and Rakovan, J. F. (2015) Structurally robust, chemically diverse: apatite and apatite supergroup minerals. *Elements* **11**, 165–170.

Irwin, J. J. and Roedder, E. (1995) Diverse origins of fluid in magmatic inclusions at Bingham (Utah, USA), Butte (Montana, USA), St. Austell (Cornwall, UK), and Ascension Island (mid-Atlantic, UK), indicated by laser microprobe analysis of Cl, K, Br, I, Ba + Te, U, Ar, Kr, and Xe. *Geochim. Cosmochim. Acta* **59**, 295–312.

Jamtveit, B. and Yardley, B. W. D. (1997) Fluid flow and transport in rocks: an overview. In *Fluid flow and transport in rocks* (eds. B. Jamtveit and B. W. D. Yardley), Chapman & Hall, London, pp. 1–14.

John, T., Layne, G. D., Haase, K. M. and Barnes, J. D. (2010) Chlorine isotope evidence for crustal recycling into the Earth's mantle. *Earth Planet. Sci. Lett.* **298**, 175–182.

Jonsson, E., Harlov, D. E., Majka, J., Högdahl, K. and Persson-Nilsson, K. (2016) Fluorapatite-monazite-allanite relations in the Grängesberg apatite-iron oxide ore district, Bergslagen, Sweden. *Am. Mineral.* **101**, 1769–1782.

Kalliomäki, H., Wagner, T., Fusswinkel, T. and Sakellaris, G. (2017) Major and trace element geochemistry of tourmalines from Archean orogenic gold deposits: proxies for the origin of gold mineralizing fluids? *Ore Geol. Rev.* **91**, 906–927.

Kaufmann, R., Long, A., Bentley, H. and David, S. (1984) Natural chlorine isotope variations. *Nature* **309**, 338–340.

Kendrick, M. A. and Burnard, P. (2013) Noble gases and halogens in fluid inclusions: a journey through the Earth's crust. In *The noble gases as geochemical tracers* (ed. P. Burnard). Springer, Heidelberg, pp. 319–370.

Kendrick, M. A., Burgess, R., Pattrick, R. A. D. and Turner, G. (2001) Fluid inclusion noble gas and halogen evidence on the origin of Cu-Porphyry mineralising fluids. *Geochim. Cosmochim. Acta* **65**, 2651–2663.

Kendrick, M. A., Mark, G. and Phillips, D. (2007) Mid-crustal fluid mixing in a Proterozoic Fe oxide-Cu-Au deposit, Ernest Henry, Australia: evidence from Ar, Kr, Xe, Cl, Br, and I. *Earth Planet. Sci. Lett.* **256**, 328–343.

Kendrick, M. A., Arculus, R., Burnard, P. and Honda, M. (2013) Quantifying brine assimilation by submarine magmas: examples from the Galápagos spreading centre and Lau Basin. *Geochim. Cosmochim. Acta* **123**, 150–165.

Kendrick, M. A., Hémond, C., Kamanetsky, V. S., Danyushevsky, L., Devey, C. W., Rodemann, T., Jackson, M. G. and Perfit, M. R. (2017) Seawater cycled throughout Earth's mantle in partially serpentinized lithosphere. *Nat. Geosci.* **10**, 222–228.

Keppler, H. and Wyllie, P. J. (1990) Role of fluids in transport and fractionation of uranium and thorium in magmatic processes. *Nature* **348**, 531–533.

Keppler, H. and Wyllie, P. J. (1991) Partitioning of Cu, Sn, Mo, W, U, and Th between melt and aqueous fluid in the systems haplogranite-H_2O-HCl and haplogranite-H_2O-HF. *Contrib Miner. Pet.* **109**, 139–150.

Kleinhanns, I. C., Whitehouse, M. J., Nolte, N., Baero, W., Wilsky, F., Hansen, B. T. and Schoenberg, R. (2015) Mode and timing of granitoid magmatism in the Västervik area (SE Sweden, Baltic Shield): Sr-Nd isotope and SIMS U-Pb age constraints. *Lithos* **212-215**, 321–337.

968 Kresten, P. (1986) The granites of the Västervik area, south-eastern Sweden. *Geological Survey of Sweden* **C814**, 35 pp.
969 Krneta, S., Ciobanu, C. L., Cook, N. J., Ehrig, K. and Kontonikas-Charos, A. (2016) Apatite at Olympic Dam, South Australia:
970 a petrogenetic tool. *Lithos* **262**, 470–485.
971 Kusebauch, C., John, T., Whitehouse, M. J. and Engvik, A. K. (2015a). Apatite as probe for the halogen composition of
972 metamorphic fluids (Bamble Sector, SE Norway). *Contrib. Mineral. Petrol.* **170**, 34.
973 Kusebauch, C., John, T., Whitehouse, M. J., Klemme, S. and Putnis, A. (2015b). Distribution of halogens between fluid and
974 apatite during fluid-mediated replacement processes. *Geochim. Cosmochim. Acta* **170**, 225–246.
975 Kusebauch, C., John, T., Barnes, J. D., Klügel, A. and Austrheim, H. O. (2015c). Halogen element and stable chlorine isotope
976 fractionation caused by fluid-rock interaction (Bamble sector, SE Norway). *J. Petrol.* **56**, 299–324.
977 Loges, A., Migdisov, A. A., Wagner, T., Williams-Jones, A. E. and Markl, G. (2013) An experimental study of the aqueous
978 solubility and speciation of Y(III) fluoride at temperatures up to 250 °C. *Geochim. Cosmochim. Acta* **123**, 403–415.
979 Luo, C., Xiao, Y., Wen, H., Ma, H., Ma, Y., Zhang, Y., Zhang, Y. and He, M. (2014) Stable isotope fractionation of chlorine
980 during the precipitation of single chloride minerals. *Appl. Geochemistry* **47**, 141–149.
981 Mansfeld, J., Beunk, F. F. and Barling, J. (2005) 1.83-1.82 Ga formation of a juvenile volcanic arc–implications from U-Pb
982 and Sm-Nd analyses of the Oskarshamn-Jönköping Belt, southeastern Sweden. *GFF* **127**, 149–157.
983 Mao, M., Rukhlov, A. S., Rowins, S. M., Spence, J. and Coogan, L. A. (2016) Apatite trace element compositions: a robust
984 new tool for mineral exploration. *Econ. Geol.* **111**, 1187–1222.
985 Marks, M. A. W., Wenzel, T., Whitehouse, M. J., Loose, M., Zack, T., Barth, M., Worgard, L., Krasz, V., Eby, G. N.,
986 Stosnach, H. and Markl, G. (2012) The volatile inventory (F, Cl, Br, S, C) of magmatic apatite: an integrated analytical
987 approach. *Chem. Geol.* **291**, 241–255.
988 Marshall, H. R. and Jiang, S-Y. (2011) Tourmaline isotopes: no element left behind. *Elements* **7**, 313–319.
989 Migdisov, A. A., Williams-Jones, A. E. and Wagner, T. (2009) An experimental study of the solubility and speciation of the
990 Rare Earth Elements (III) in fluoride- and chloride-bearing aqueous solutions at temperatures up to 300 °C. *Geochim.*
991 *Cosmochim. Acta* **73**, 7087–7109.
992 Migdisov, A., Williams-Jones, A. E., Brugger, J. and Caporuscio, F. A. (2016) Hydrothermal transport, deposition, and
993 fractionation of the REE: experimental data and thermodynamic calculations. *Chem. Geol.* **439**, 13–42.
994 Miron, G. D., Wagner, T., Wälle, M. and Heinrich, C. A. (2013) Major and trace-element composition and pressure-
995 temperature evolution of rock-buffered fluids in low-grade accretionary-wedge metasediments, Central Alps. *Contrib. to*
996 *Mineral. Petrol.* **165**, 981–1008.
997 Musashi, M., Markl, G. and Kreulen, R. (1998) Stable chlorine-isotope analysis of rock samples: new aspects of chlorine
998 extraction. *Anal. Chim. Acta* **362**, 261–269.

Nahnybida, T., Gleeson, S. A., Rusk, B. G. and Wassenaar, L. I. (2009) Cl/Br ratios and stable chlorine isotope analysis of magmatic-hydrothermal fluid inclusions from Butte, Montana and Bingham Canyon, Utah. *Miner. Depos.* **44**, 837–848.

Nolte, N., Kleinhanns, I. C., Baero, W. and Hansen, B. T. (2011) Petrography and whole-rock geochemical characteristics of Västervik granitoids to syenitoids, southeast Sweden: constraints on petrogenesis and tectonic setting at the southern margin of the Svecofennian domain. *GFF* **133**, 173–194.

Ohmoto, H. (1972) Systematics of sulfur and carbon isotopes in hydrothermal ore deposits. *Econ. Geol.* **67**, 551–578.

Pan, Y. and Fleet, M. E. (2002) Compositions of the apatite-group minerals: substitution mechanisms and controlling factors. *Rev. Mineral. Geochemistry* **48**, 13–49.

Pasero, M., Kampf, A. R., Ferraris, C., Pekov, I. V, Rakovan, J. and White, T. J. (2010) Nomenclature of the apatite supergroup minerals. *Eur. J. Mineral.* **22**, 163–179.

Pettke, T., Oberli, F., Audétat, A., Guillong, M., Simon, A. C., Hanley, J. J. and Klemm, L. M. (2012) Recent developments in element concentration and isotope ratio analysis of individual fluid inclusions by laser ablation single and multiple collector ICP-MS. *Ore Geol. Rev.* **44**, 10–38.

Piccoli, P. M. and Candela, P. A. (1994) Apatite in felsic rocks: a model for the estimation of initial halogen concentrations in the Bishop tuff (Long Valley) and Tuolumne intrusive suite (Sierra Nevada batholith) magmas. *Am. J. Sci.* **294**, 92–135.

Piccoli, P. M. and Candela, P. A. (2002) Apatite in igneous systems. *Rev. Mineral. Geochemistry* **48**, 255–292.

Pyle, J. M., Spear, F. S., Rudnick, R. L. and Mcdonough, W. F. (2001) Monazite – xenotime – garnet equilibrium in metapelites and a new monazite – garnet thermometer. *J. Petrol.* **42**, 2083–2107.

Rasmussen, K. L. and Mortensen, J. K. (2013) Magmatic petrogenesis and the evolution of (F: Cl: OH) fluid composition in barren and tungsten skarn-associated plutons using apatite and biotite compositions: case studies from the northern Canadian Cordillera. *Ore Geol. Rev.* **50**, 118–142.

Rauchenstein-Martinek, K., Wagner, T., Wälle, M., Heinrich, C. A. and Arlt, T. (2016) Chemical evolution of metamorphic fluids in the Central Alps, Switzerland: insight from LA-ICPMS analysis of fluid inclusions. *Geofluids* **16**, 877–908.

Rønsbo, J. G. (2008) Apatite in the Ilímaussaq alkaline complex: occurrence, zonation and compositional variation. *Lithos* **106**, 71–82.

Rudnick, R. L. and Gao, S. (2003) Composition of the continental crust. In *Treatise on Geochemistry* (eds. H. D. Holland and K. K. Turekian), Elsevier Ltd., Oxford, pp. 1–64.

Rusk, B. G., Reed, M. H., Dilles, J. H., Klemm, L. M. and Heinrich, C. A. (2004) Compositions of magmatic hydrothermal fluids determined by LA-ICP-MS of fluid inclusions from the porphyry copper-molybdenum deposit at Butte, MT. *Chem. Geol.* **210**, 173–199.

1029 Schauble, E. A, Rossman, G. R. and Taylor, H. P. J. (2003) Theoretical estimates of equilibrium chlorine-isotope
1030 fractionations. *Geochim Cosmochim Acta* **67**, 3267–3281.
1031 Schisa, P., Boudreau, A., Djon, L., Tchalikian, A. and Corkery, J. (2015) The Lac Des Iles Palladium Deposit, Ontario,
1032 Canada. Part II. Halogen variations in apatite. *Miner. Depos.* **50**, 339–355.
1033 Seal, R. R. (2006) Sulfur isotope geochemistry of sulfide minerals. *Rev. Mineral. Geochemistry* **61**, 633–677.
1034 Selverstone, J. and Sharp, Z. D. (2013) Chlorine isotope constraints on fluid-rock interactions during subduction and
1035 exhumation of the Zermatt-Saas ophiolite. *Geochemistry, Geophys. Geosystems* **14**, 4370–4391.
1036 Selverstone, J. and Sharp, Z. D. (2015) Chlorine isotope behavior during prograde metamorphism of sedimentary rocks. *Earth*
1037 *Planet. Sci. Lett.* **417**, 120–131.
1038 Seo, J. H., Guillong, M., Aerts, M., Zajacz, Z. and Heinrich, C. A. (2011) Microanalysis of S, Cl, and Br in fluid inclusions by
1039 LA-ICP-MS. *Chem. Geol.* **284**, 35–44.
1040 Sharp, Z. D., Barnes, J. D., Brearley, A. J., Chaussidon, M., Fischer, T. P. and Kamenetsky, V. S. (2007) Chlorine isotope
1041 homogeneity of the mantle, crust and carbonaceous chondrites. *Nature* **446**, 1062–1065.
1042 Shvarov, Y. V. (2008) HCh: New potentialities for the thermodynamic simulation of geochemical systems offered by
1043 windows. *Geochem. Intern.* **46**, 834–839.
1044 Simons, B., Shail, R. K. and Andersen, J. C. O. (2016) The petrogenesis of the Early Permian Variscan granites of the
1045 Cornubian Batholith: lower plate post-collisional peraluminous magmatism in the Rhenohercynian Zone of SW England.
1046 *Lithos* **260**, 76–94.
1047 Sisson, V. B. (1987) Halogen chemistry as an indicator of metamorphic fluid interaction with the Ponder pluton, Coast
1048 Plutonic Complex, British Columbia, Canada. *Contrib. to Mineral. Petrol.* **95**, 123–131.
1049 Slack, J. F. (1996) Tourmaline associations with hydrothermal ore deposits. *Rev. Mineral. Geochemistry* **33**, 559–644.
1050 Slack, J. F. and Trumbull, R. B. (2011) Tourmaline as a recorder of ore-forming processes. *Elements* **7**, 321–326.
1051 Spandler, C., Pettke, T. and Rubatto, D. (2011) Internal and external fluid sources for eclogite facies veins in the Monviso
1052 meta-ophiolite, Western Alps: implications for fluid flow in subduction zones. *J. Petrol.* **52**, 1207–1236.
1053 Spear, F. S. and Pyle, J. M. (2002) Apatite, monazite, and xenotime in metamorphic rocks. *Rev. Mineral. Geochemistry* **48**,
1054 293–335.
1055 Stephens, M. B., Ripa, M., Lundström, I., Persson, L., Bergman, T., Ahl, M., Wahlgren, C.-H., Persson, P.-O. and Wickström,
1056 L. (2009) Synthesis of the bedrock geology in the Bergslagen region, Fennoscandian Shield, south-central Sweden.
1057 *Geological Survey of Sweden* **Ba 58**, 259 pp.
1058 Stock, M. J., Humphreys, M. C. S., Smith, V. C., Johnson, R. D. and Pyle, D. M. (2015) New constraints on electron-beam
1059 induced halogen migration in apatite. *Am. Mineral.* **100**, 281–293.

Stormer, J. C., Pierson, M. L. and Tacker, R. C. (1993) Variation of F and Cl X-ray intensity due to anisotropic diffusion in apatite during electron microprobe analysis. *Am. Mineral.* **78**, 641–648.

Sultan, L., Claesson, S. and Plink-Björklund, P. (2005) Proterozoic and Archaean ages of detrital zircon from the Palaeoproterozoic Västervik Basin, SE Sweden: implications for provenance and timing of deposition. *GFF* **127**, 17–24.

Svensen, H., Jamtveit, B., Banks, D. A. and Austrheim, H. (2001) Halogens contents of eclogite facies fluid inclusions and minerals: Caledonides, Western Norway. *J. Metamorph. Geol.* **19**, 165–178.

Tacker, C. and Stormer, J. C. (1989) A thermodynamic model for apatite solid solutions, applicable to high-temperature geologic problems. *Am. Mineral.* **74**, 877–888.

Taylor, H.P. Jr. (1997) Oxygen and hydrogen isotope relationships in hydrothermal mineral deposits. In *Geochemistry of hydrothermal ore deposits* (ed. H. L. Barnes). John Wiley & Sons, Canada, pp. 229–303.

Timofeev, A., Migdisov, A. A. and Williams-Jones, A. E. (2015) An experimental study of the solubility and speciation of niobium in fluoride-bearing aqueous solutions at elevated temperature. *Geochim. Cosmochim. Acta* **158**, 103–111.

Treloar, P. J. and Colley, H. (1996) Variations in F and Cl contents in apatites from magnetite-apatite ores in northern Chile, and their ore-genetic implications. *Mineral. Mag.* **60**, 285–301.

Ulrich, T. and Gunther, D. (2002) The evolution of a Porphyry Cu-Au deposit, based on LA-ICP-MS analysis of fluid inclusions: Bajo de la Alumbrera, Argentina. *Econ. Geol.* **96**, 1743–1774.

Uytenbogaardt, W. (1960) Uranium mineralization in the Västervik area. *International Geological Congress* **15**, 114–122.

Valley, P. M., Fisher, C. M., Hanchar, J. M., Lam, R. and Tubrett, M. (2010) Hafnium isotopes in zircon: a tracer of fluid-rock interaction during magnetite-apatite ("Kiruna-type") mineralization. *Chem. Geol.* **275**, 208–220.

Wagner, T., Fusswinkel, T., Wälle, M. and Heinrich, C. A. (2016) Microanalysis of fluid inclusions in crustal hydrothermal systems using laser ablation methods. *Elements* **12**, 323–328.

Webster, J. D. and Piccoli, P. (2015) Magmatic apatite: a powerful, yet deceptive, mineral. *Elements* **11**, 177–182.

Webster, J. D., Tappen, C. M. and Mandeville, C. W. (2009) Partitioning behavior of chlorine and fluorine in the system apatite-melt-fluid. II: Felsic silicate systems at 200 MPa. *Geochim. Cosmochim. Acta* **73**, 559–581.

Weis, P. (2014) The physical hydrology of ore-forming magmatic-hydrothermal systems. *Econ. Geol. Special Publication* **18**, 59–75.

Weis, P. (2015) The dynamic interplay between saline fluid flow and rock permeability in magmatic-hydrothermal systems. *Geofluids* **15**, 350–371.

Wikström, A. and Andersson, U. B. (2004) The Småland-Värmland belt – geological features of the Småland-Värmland belt along the Svecofennian margin, part I: from the Loftahammar to the Tiveden-Askersund areas. *Geol. S. Finl.* **37**, 22–38.

Williams-Jones, A. E. and Migdisov, A. A. (2014) Experimental constraints on the transport and deposition of metals in ore-forming hydrothermal systems. *Econ. Geol. Special Publication* **18**, 77–95.

Yang, W. Bin, Niu, H. C., Shan, Q., Sun, W. D., Zhang, H., Li, N. B., Jiang, Y. H. and Yu, X. Y. (2014) Geochemistry of magmatic and hydrothermal zircon from the highly evolved Baerzhe alkaline granite: implications for Zr-REE-Nb mineralization. *Miner. Depos.* **49**, 451–470.

Yardley, B. W. D. (1985) Apatite composition and the fugacities of HF and HCl in metamorphic fluids. *Mineral. Mag.* **49**, 77–79.

Zhu, C. and Sverjensky, D. A. (1991) Partitioning of F-Cl-OH between minerals and hydrothermal fluids. *Geochim. Cosmochim. Acta* **55**, 1837–1858.

Zhu, C. and Sverjensky, D. A. (1992) F-Cl-OH partitioning between biotite and apatite. *Geochim. Cosmochim. Acta* **56**, 3435–3467.

Zirner, A. L. K., Marks, M. A. W., Wenzel, T., Jacob, D. E. and Markl, G. (2015) Rare earth elements in apatite as a monitor of magmatic and metasomatic processes: The Ilímaussaq complex, South Greenland. *Lithos* **228–229**, 12–22.

Figure captions

Fig. 1. Geological map of the Västervik region with black stars indicating the location of the exposed REE mineralised areas. Modified after Andersson et al. (2018b). The lower-left inset map portrays the regional geology of southern Sweden, redrawn from Andersen et al. (2009). LLDZ: Loftahammar-Linköping Deformation Zone (Beunk and Page, 2001); TIB: Transscandinavian Igneous Belt (Gorbatschev, 2004); OJB: Oskarshamn-Jönköping Belt (Mansfeld et al., 2005).

Fig. 2. Field photographs, photomicrographs, and BSE images illustrating the occurrence and key petrographic features of fluorapatite in the Olserum-Djupedal REE-phosphate mineralisation. (A) Field photograph showing biotite-fluorapatite-dominated interconnected veins in the metasedimentary host rock in the Olserum area. The abundant white spots inside the veins are the primary fluorapatite crystals. (B) BSE image showing a larger fluorapatite crystal with a core rich in inclusions of monazite-(Ce) and xenotime-(Y), and with rims devoid of monazite-(Ce) and xenotime-(Y) inclusions. Note also the coarser xenotime-(Y) grains at the outer edges of the fluorapatite crystal. (C) BSE image depicting part of a larger fluorapatite crystal with an inclusion-rich core (lower right of the image) with a rim containing fewer and coarser monazite-(Ce) and xenotime-(Y) grains. (D) BSE image illustrating part of a larger fluorapatite crystal with recrystallised domains along the crystal margin. Note the overall absence of monazite-(Ce) and xenotime-(Y) inclusions in the recrystallised grains. (E) Reflected polarised-light microphotograph of primary fluorapatite associated with extensive replacement of brown-grey magnetite by white-grey hematite (martitisation) in the surrounding mineral groundmass. (F) BSE image depicting the replacement of a large primary monazite-(Ce) crystal in the Djupedal area by secondary fluorapatite and minor allanite-(Ce) – ferriallanite-(Ce) along the crystal margin. Mineral abbreviations: Aln: allanite–ferriallanite; Bt: biotite; F-ap: fluorapatite; Ged: gedrite; Hem: hematite; Mag: magnetite; Mnz: monazite; Qz: quartz; Xtm: xenotime.

Fig. 3. Diagrams comparing (A) the Cl, and (B) the F concentrations in fluorapatite from the Olserum-Djupedal REE-phosphate mineralisation as determined by SIMS and EPMA.

Fig. 4. Diagram displaying the linear correlation between the Na and ∑(REE+Y) concentrations in fluorapatite from the Olserum-Djupedal REE-phosphate mineralisation.

Fig. 5. Average normalised (upper continental crust; Rudnick and Gao, 2003) (REE+Y) distribution patterns of all fluorapatite types from the Olserum-Djupedal REE-phosphate mineralisation. Characteristic features include a general enrichment in the MREE, a steep LREE slope, a shallower HREE slope, a pronounced Eu anomaly, and a moderate Y anomaly.

Fig. 6. Diagrams displaying the normalised La/Sm, La/Yb, and Gd/Yb ratios of fluorapatite from the Olserum-Djupedal REE-phosphate mineralisation. (A) $(Gd/Yb)_N$ vs. $(La/Sm)_N$. (B) $(Gd/Yb)_N$ vs. $(La/Yb)_N$. Primary and secondary fluorapatite define well-separated trends in both diagrams.

Fig. 7. Diagram displaying the variation in Sr and Mn concentrations of fluorapatite from the Olserum-Djupedal REE-phosphate mineralisation. The compositional fields are adopted from Belousova et al. (2002).

Fig. 8. Diagrams illustrating the halogen composition of fluorapatite from the Olserum-Djupedal REE-phosphate mineralisation. (A) An enlarged part of the F-Cl-OH ternary diagram showing the major halogen composition of fluorapatite. (B) Diagram displaying the $(La/Sm)_N$ ratio as a function of the F concentration. The symbols that have an individual uncertainty interval assigned represent F concentrations measured using SIMS analysis. Symbols lacking an uncertainty interval represent F concentrations measured with EPMA and have an average uncertainty as shown. (C) Diagram showing the Br concentration as a function of the I concentration based on SIMS data.

Fig. 9. The $\delta^{37}Cl$ (relative to SMOC) composition of the analysed fluorapatite of the Olserum-Djupedal REE-phosphate mineralisation, compared to potential fluid sources and natural reservoirs. The data sources include: evaporites (Eggenkamp et al., 1995; Eastoe et al., 2007); formation waters/brines (Eastoe et al. 1999, 2001; Sharp et al., 2007); sedimentary pore fluids (Barnes and Sharp, 2017, and references therein); marine shales (Selverstone and Sharp, 2015); marine sediments (Arcuri and Brimhall, 2003;

Barnes et al., 2008, 2009); metasedimentary rocks (John et al., 2010; Selverstone and Sharp, 2013); mantle/MORB (Sharp et al., 2007, grey bar indicates values for oceanic island basalts (OIB) potentially sourced from enriched mantle; John et al., 2010); magmatic fluids and fluids associated with iron-oxide-copper-gold (IOCG) and iron-oxide apatite (IOA) deposits (Eastoe and Guilbert, 1992; Eggenkamp, 1994; Musashi et al., 1998; Banks et al., 2000a, 2000b, Chiaradia et al., 2006; Gleeson and Smith, 2009; Nahnybida et al., 2009); metasomatic fluids in Norway (Kusebauch et al., 2015a).

Fig. 10. Diagrams showing the $\delta^{37}Cl$ composition as a function of (A) F concentration, and (B) the $(La/Sm)_N$ ratio.

Fig. 11. Diagram plotting the molar Br/Cl ratio as a function of the I/Cl ratio for fluorapatite from the Olserum-Djupedal REE-phosphate mineralisation. The porphyry-type magmatic field is defined by data from Irwin and Roedder (1995), Kendrick et al. (2001) and Seo et al. (2011) and the S-type magmatic fluid field by data from Böhlke and Irwin (1992), Irwin and Roedder (1995), Banks et al. (2000a, 2000b), and Seo et al. (2011). The mantle field is defined by data from Kendrick et al. (2013, 2017). Fluid inclusion compositions for Na-Fe-K-Ca, Ca-Na, and Na-Ca brines from the Olserum-Djupedal REE-phosphate mineralisation were taken from Andersson (2019). The average values for the bulk continental crust and upper continental crust are adopted from Rudnick and Gao (2003). SET is the seawater evaporation trend. Modified after Fusswinkel et al. (2018). The reconstructed fluid composition field was calculated for a fluid salinity range of 1-20 wt% NaCl using average Br and I concentrations of the granite-hosted fluorapatite and partition coefficients ($D^{Br}_{apatite\text{-}fluid}$ and $D^{I}_{apatite\text{-}fluid}$) from Kusebauch et al. (2015b).

Fig. 12. Diagrams displaying halogen fugacity values in fluids associated with the Olserum-Djupedal REE-phosphate mineralisation, calculated from the fluorapatite composition at temperatures of 600 °C and 650 °C (only granite-hosted fluorapatite) and 200 MPa. The values are compared to those calculated from the composition (F, Cl, and OH contents) of hydrothermal biotite (Andersson et al., 2018b). (A) $\log(f_{HF}/f_{HCl})$ vs. $\log(f_{H2O}/f_{HCl})$ (B) $\log(f_{HF}/f_{HCl})$ vs. $\log(f_{H2O}/f_{HF})$.

Fig. 13. Diagram showing the normalised Y/Ho ratios of fluorapatite as a function of the calculated $\log(f_{HF}/f_{HCl})$ values.

Fig. 14. Diagram portraying the result of the Rayleigh fractionation modelling of the Cl isotope partitioning between the co-existing fluid and the Cl-bearing minerals (fluorapatite, biotite, and gedrite) in the Olserum-Djupedal REE-phosphate mineralisation. Here, essentially the process of primary hydrothermal fluids flowing out from the TIB granitic pluton into the adjacent metasedimentary rocks is modelled. The model assumes a starting fluid ($\delta^{37}Cl^{0}_{fluid}$) composition of +1.4‰. The lines represent different fractionation factors (α) proposed in the literature, and assumed to be valid at high temperatures (1.0002, amphibole-fluid at 700 °C, Cisneros, 2013; 1.0005 and 1.0010, bulk-fluid at 600 °C, Kusebauch et al., 2015b; 1.0019, scapolite-fluid at 500 °C, Bernal et al., 2017).

Table 1

Table 1. Information on samples used for this study.

Type	Sample	Mineral association
Primary fluorapatite, Granite-hosted	OLR12003-117.4	Biotite, magnetite, fluorapatite, monazite-(Ce), xenotime-(Y), quartz, ilmenite, muscovite, chlorite, uraninite, hematite, rutile
Primary fluorapatite, Olserum	OLR12003-172.8	Fluorapatite, biotite, magnetite, monazite-(Ce), xenotime-(Y), quartz, albite, andalusite, chlorite, pyrite, chalcopyrite, zircon, hematite, calcite
Primary fluorapatite, Olserum	OLR12005-105.7	Fluorapatite, biotite, quartz, monazite-(Ce), xenotime-(Y), magnetite, ilmenite, (REE,Y,Th,U,Ca)-(Nb,Ta)-oxide, pyrrhotite, chalcopyrite, uraninite, columbite-(Fe), galena, chlorite, calcite
Primary fluorapatite, Olserum	OLR12005-83.4	Fluorapatite, gedrite, biotite, cordierite, quartz, monazite-(Ce), xenotime-(Y), magnetite, ilmenite, pyrite, pyrrhotite, (staurolite), chlorite, rutile
Primary fluorapatite, Bersummen	BER01	Fluorapatite, biotite, quartz, xenotime-(Y), monazite-(Ce), magnetite, gedrite, chalcopyrite, pyrite, staurolite, andalusite, chlorite, unspecified U-mineral
Primary fluorapatite, Djupedal	DJU17	Fluorapatite, biotite, quartz, monazite-(Ce), xenotime-(Y), magnetite, pyrite, thorite, columbite-(Fe)
Primary altered fluorapatite, Olserum	OLR13	Biotite, fluorapatite, magnetite, hematite, monazite-(Ce), xenotime-(Y), quartz, pyrite
Secondary fluorapatite, Djupedal	DJU06	Xenotime-(Y), monazite-(Ce), biotite, quartz, cordierite, magnetite, ilmenite, fluorapatite, allanite-(Ce)–ferriallanite-(Ce), clinozoisite, hematite, chlorite, bastnäsite-(Ce),
Secondary fluorapatite, Djupedal	DJU08	Monazite-(Ce), biotite, magnetite, quartz, muscovite, ilmenite, fluorapatite, allanite-(Ce)–ferriallanite-(Ce), uraninite, thorite, titanite, rutile, chlorite, fluorite
Secondary fluorapatite, Djupedal	DJU22-1	Biotite, allanite-(Ce)–ferriallanite-(Ce), magnetite, monazite-(Ce), xenotime-(Y), quartz, muscovite, ilmenite, uvite, fluorapatite, clinozoisite, ferberite, scheelite, rutile, titanite, thorite, staurolite, chlorite, bastnäsite-(Ce)
Secondary fluorapatite, Olserum	OLR12003-156.6	Biotite, magnetite, xenotime-(Y), monazite-(Ce), quartz, muscovite, (REE,Y,Th,U,Ca)-(Nb,Ta)-oxide, ilmenite, columbite-(Fe), uraninite, zircon, U-Th silicates, rutile

Table 2

Table 2. Average compositions of analysed fluorapatite samples in the Olserum-Djupedal REE-phosphate mineralisation.

Type	Primary fluorapatite, Olserum		Primary fluorapatite, Olserum		Primary fluorapatite, Olserum		Primary fluorapatite, Djupedal		Primary fluorapatite, Bersummen		Granite-hosted fluorapatite, Olserum		Primary altered fluorapatite, Olserum		Secondary fluorapatite, Djupedal		Secondary fluorapatite, Djupedal		Secondary fluorapatite, Djupedal		Secondary fluorapatite, Olserum	
Sample	OLR12003-172.8		OLR12005-83.4		OLR12005-105.7		DJU17		BER01		OLR12003-117.4		OLR13		DJU06		DJU08		DJU22		OLR12003-156.6	
	Average	SD	Average	SD	Average	SD	Average	SD	Average	SD	Average	SD	Average	SD	Average	SD	Average	SD	Average	SD	Average	SD
EPMA, wt%																						
CaO	54.62	*0.69*	54.67	*1.04*	55.23	*0.72*	56.2	*1.05*	54.87	*1.06*	54.84	*1.01*	54.51	*1.08*	54.25	*0.84*	55.63	*1.03*	55.34	*1.36*	54.77	*1.05*
Na_2O	0.09	*0*	0.10	*0.01*	0.09	*0.01*	<LOD		0.09		0.10	*0.01*	<LOD		<LOD		<LOD		<LOD		0.10	*0.01*
FeO	0.21	*0.06*	0.63	*0.06*	0.27	*0.08*	0.24	*0.05*	0.31	*0.08*	0.11	*0.03*	0.49	*0.14*	0.31	*0.14*	0.16	*0.13*	0.27	*0.15*	0.38	*0.09*
MnO	0.53	*0.11*	<LOD		0.43		<LOD		<LOD		<LOD		<LOD		<LOD		<LOD		0.36	*0.01*	<LOD	
P_2O_5	41.14	*0.78*	42.89	*0.63*	41.56	*1.55*	42.11	*0.71*	43.85	*1.13*	42.41	*1.88*	42.7	*0.58*	40.66	*0.73*	42.89	*1.31*	40.87	*0.63*	42.19	*1.41*
SiO_2	<LOD		<LOD		0.30		<LOD		0.21		<LOD		0.19		0.16	*0.06*	0.56		0.39	*0.22*	<LOD	
Y_2O_3	0.17	*0.10*	0.12	*0.02*	0.12	*0.02*	0.12	*0.03*	0.11		0.19	*0.11*	<LOD		<LOD		0.10	*0*	<LOD		0.16	*0.04*
La_2O_3	<LOD		<LOD		<LOD		<LOD		<LOD		<LOD		<LOD		<LOD		<LOD		<LOD		<LOD	
Ce_2O_3	<LOD		<LOD		0.39	-	<LOD		<LOD		<LOD		<LOD		<LOD		<LOD		<LOD		<LOD	
Pr_2O_3	<LOD		<LOD		<LOD		<LOD		<LOD		<LOD		<LOD		<LOD		<LOD		<LOD		0.35	
Nd_2O_3	<LOD		<LOD		<LOD		<LOD		<LOD		<LOD		<LOD		<LOD		<LOD		<LOD		<LOD	
Sm_2O_3	<LOD		0.23		<LOD		<LOD		<LOD		<LOD		<LOD		<LOD		<LOD		<LOD		<LOD	
Gd_2O_3	<LOD		<LOD		0.23	-	<LOD		<LOD		<LOD		<LOD		0.25		<LOD		<LOD		<LOD	
F	3.73	*0.22*	3.22	*0.27*	3.14	*0.25*	2.99	*0.24*	3.11	*0.17*	3.70	*0.21*	3.34	*0.28*	2.79	*0.24*	3.20	*0.19*	3.04	*0.26*	3.53	*0.21*
Cl	0.12	*0.03*	0.40	*0.06*	0.25	*0.03*	0.57	*0.12*	0.43	*0.04*	0.08	*0.02*	0.27	*0.07*	0.70	*0.09*	0.42	*0.07*	0.81	*0.09*	0.13	*0.02*
H_2O[a]	0.06	*0.04*	0.20	*0.11*	0.16	*0.09*	0.24	*0.09*	0.23	*0.08*	0.02	*0.05*	0.09	*0.08*	0.22	*0.07*	0.23	*0.06*	0.12	*0.10*	0.21	*0.07*
LA-ICP-MS, ppm																						
Na	454	*78*	697	*131*	434	*24*	232	*15*	423	*52*	511	*43*	447	*47*	194	*21*	185	*27*	194	*14*	602	*103*
Mg	151	*31*	613	*35*	274	*17*	161	*28*	281	*26*	59	*5.8*	348	*99*	195	*40*	143	*28*	174	*30*	252	*13*
Si	166	*48*	147	*32*	240	*139*	231	*43*	166	*53*	174	*29*	171	*35*	350	*244*	298	*59*	254	*139*	262	*91*
P	195053	*8953*	213750	*7620*	196333	*6240*	207056	*6245*	220333	*5486*	212222	*12816*	196000	*5087*	202300	*11667*	209000	*7079*	215944	*9521*	201250	*4683*
S	270	*38*	185	*49*	197	*23*	250	*21*	215	*55*	206	*34*	235	*31*	194	*21*	177	*23*	203	*20*	210	*38*
^{42}Ca[b]	393895	*5425*	398125	*6479*	401778	*10636*	409889	*10318*	396267	*9816*	391259	*8663*	396000	*9318*	390750	*9931*	405850	*8229*	402333	*10392*	387750	*5800*
^{43}Ca	I.STD		I.STD		I.STD		I.STD		I.STD		I.STD		I.STD		I.STD		I.STD		I.STD		I.STD	
Sc	1.71	*0.40*	4.04	*0.45*	1.77	*0.23*	0.6	*0.11*	0.94	*0.11*	0.27	*0.07*	2.44	*0.77*	0.54	*0.16*	0.37	*0.12*	0.06	*0.02*	5.55	*0.94*
V	0.09	*0.01*	0.03	*0.01*	0.04	*0.01*	0.06	*0.01*	0.07	*0.03*	0.09	*0.03*	0.18	*0.16*	0.07	*0.02*	0.21	*0.49*	0.07	*0.05*	<0.15	
Mn	1239	*101*	378	*20*	485	*17*	417	*15*	489	*28*	417	*16*	188	*65*	625	*35*	419	*45*	279	*27*	1718	*248*
Fe	1507	*259*	4498	*256*	2215	*283*	1652	*260*	2487	*90*	584	*54*	3633	*1089*	2060	*501*	1277	*236*	1580	*188*	2635	*152*
Co	0.08	*0.03*	0.16	*0.02*	0.09	*0.02*	0.04	*0.01*	0.09	*0.02*	0.04	*0.01*	0.16	*0.04*	0.05	*0.01*	0.06	*0.04*	0.06	*0.02*	0.24	*0.24*
As	8.13	*0.89*	8.05	*1.5*	6.64	*0.89*	17.8	*1.2*	6.74	*1.86*	12.2	*2.38*	6.51	*2.58*	18.9	*2.42*	21.3	*2.93*	15.8	*1.37*	6.85	*0.77*
Sr	79	*2.4*	72	*2.7*	100	*4.1*	118	*7.6*	99	*5.0*	102	*2.2*	435	*224*	188	*18*	105	*6.2*	83	*3.1*	88	*3.9*
Y	821	*101*	1125	*249*	758	*60*	447	*88*	629	*102*	907	*70*	756	*103*	447	*98*	582	*162*	479	*27*	1464	*404*
La	59	*12*	65	*19*	51	*7.1*	26	*6.2*	31	*6.6*	66	*9.3*	46	*9.2*	45	*11*	44	*9.5*	42	*7.1*	90	*31*
Ce	281	*45*	347	*96*	240	*22*	161	*28*	193	*31*	306	*31*	229	*32*	176	*37*	185	*41*	170	*19*	405	*106*
Pr	59	*7.5*	82	*18*	54	*3.5*	39	*5.5*	52	*6.7*	61	*4.7*	54	*7.8*	32	*6.3*	35	*8.2*	32	*2.8*	79	*17*
Nd	396	*40*	627	*118*	398	*32*	293	*37*	427	*47*	410	*26*	416	*63*	203	*37*	226	*52*	201	*15*	516	*93*
Sm	245	*27*	400	*47*	276	*27*	178	*18*	315	*24*	226	*14*	294	*34*	98	*17*	110	*27*	96	*6.0*	243	*46*
Eu	3.72	*0.37*	8.15	*0.85*	6.32	*0.48*	10.1	*1.0*	8.46	*0.68*	3.31	*0.24*	9.41	*1.11*	6.52	*1.11*	7.53	*2.26*	5.89	*0.42*	3.17	*0.53*
Gd	365	*67*	560	*68*	397	*33*	247	*28*	421	*39*	328	*20*	436	*42*	152	*26*	163	*39*	147	*8.8*	355	*66*
Tb	53	*8.5*	81	*11*	57	*4.3*	35	*4.7*	58	*5.8*	50	*3.4*	62	*6.1*	24	*4.3*	26	*7.0*	24	*1.5*	56	*12*
Dy	255	*34*	385	*67*	265	*19*	155	*25*	252	*31*	260	*20*	275	*32*	131	*26*	148	*41*	129	*7.9*	322	*78*

Ho	34	*4.2*	50	*11*	33	*2.5*	19	*3.8*	30	*4.7*	36	*3.2*	33	*4.8*	18	*3.9*	23	*6.4*	19	*1.3*	52	*14*
Er	69	*8.8*	102	*27*	66	*5.7*	37	*8.4*	56	*10*	79	*8.1*	65	*11*	38	*9.1*	53	*16*	42	*3.0*	128	*37*
Tm	6.59	*0.94*	9.71	*2.71*	6.48	*0.7*	3.51	*0.87*	5.11	*0.94*	8.1	*0.95*	6.23	*1.07*	3.71	*0.96*	5.49	*1.75*	4.09	*0.37*	13.9	*4.74*
Yb	33	*5.5*	50	*15*	34	*4.0*	18	*4.8*	25	*4.7*	44	*5.7*	32	*5.6*	20	*5.5*	30	*10*	21	*2.5*	84	*31*
Lu	3.38	*0.68*	4.95	*1.56*	3.48	*0.47*	1.83	*0.53*	2.38	*0.48*	4.69	*0.65*	3.2	*0.63*	2.07	*0.6*	3.11	*1.12*	2.09	*0.32*	9.75	*3.85*
Pb	2.89	*0.44*	3.16	*0.31*	1.83	*0.21*	2.1	*1.57*	4.39	*0.46*	2.25	*0.41*	6.15	*0.56*	2.64	*0.85*	2.73	*0.38*	2.65	*0.29*	6.69	*0.69*
U	2.09	*0.94*	15.2	*5.6*	4.35	*1.58*	1.61	*1.21*	7.13	*4.07*	2.16	*0.92*	5.12	*2.14*	2.93	*1.3*	1.9	*0.93*	1.21	*0.49*	6.65	*3.53*
∑REE+Y	2683	*332*	3897	*735*	2645	*179*	1670	*251*	2504	*310*	2789	*207*	2717	*319*	1398	*278*	1640	*414*	1413	*89*	3821	*924*
$(Y/Ho)_N$	0.967	*0.015*	0.891	*0.026*	0.912	*0.019*	0.932	*0.017*	0.838	*0.019*	0.986	*0.029*	0.896	*0.022*	0.965	*0.015*	1.017	*0.029*	1.001	*0.025*	1.118	*0.042*
$(Y/Y^*)_N$	0.741	*0.027*	0.672	*0.025*	0.671	*0.023*	0.679	*0.018*	0.595	*0.019*	0.783	*0.024*	0.650	*0.012*	0.764	*0.019*	0.852	*0.043*	0.816	*0.023*	0.960	*0.041*
$(La/Yb)_N$	0.112	*0.014*	0.081	*0.006*	0.094	*0.004*	0.093	*0.009*	0.076	*0.006*	0.095	*0.007*	0.091	*0.007*	0.147	*0.018*	0.098	*0.020*	0.126	*0.015*	0.070	*0.013*
$(La/Sm)_N$	0.037	*0.006*	0.024	*0.004*	0.028	*0.005*	0.022	*0.003*	0.015	*0.002*	0.044	*0.005*	0.024	*0.006*	0.070	*0.010*	0.062	*0.009*	0.066	*0.010*	0.055	*0.009*
$(Gd/Yb)_N$	5.399	*1.008*	5.612	*0.713*	5.757	*0.819*	7.000	*1.021*	8.269	*0.753*	3.709	*0.307*	6.739	*0.885*	3.862	*0.416*	2.783	*0.539*	3.486	*0.327*	2.208	*0.429*
$(Eu/Eu^*)_N$	0.053	*0.005*	0.073	*0.003*	0.080	*0.003*	0.204	*0.014*	0.099	*0.003*	0.051	*0.002*	0.110	*0.004*	0.221	*0.009*	0.232	*0.018*	0.206	*0.006*	0.045	*0.003*
SIMS																						
$\delta^{37}Cl$ (‰)	0.58	*0.47*	0.03	*0.22*	0.59	*0.24*	-0.51	*0.12*	-0.51	*0.13*	0.98	*0.94*	-0.18	*0.28*	-0.51	*0.15*	-0.27	*0.23*	-0.07	*0.11*	-0.1	*0.51*
F (ppm)	34922	*430*	31937	*775*	32508	*225*	29273	*997*	N.A.		37490	*971*	34840	*843*	29011	*722*	30902	*846*	30259	*332*	32227	*685*
Cl (ppm)	1030	*194*	3540	*595*	2863	*150*	5294	*691*	N.A.		840	*143*	2547	*607*	6768	*550*	3748	*534*	7951	*946*	1116	*68*
Br (ppm)	1.89	*0.33*	1.66	*0.18*	1.59	*0.14*	19.2	*3.03*	N.A.		1.10	*0.23*	17.2	*4.75*	11.6	*2.16*	10.5	*2.46*	25.6	*3.30*	3.86	*0.69*
I (ppm)	0.59	*0.06*	0.65	*0.04*	0.63	*0.05*	0.46	*0.17*	N.A.		0.76	*0.09*	0.57	*0.05*	0.42	*0.04*	0.43	*0.03*	0.61	*0.35*	0.94	*0.11*
Br/Cl · 10^{-3} (molar)	0.82	*0.12*	0.22	*0.04*	0.25	*0.02*	1.61	*0.10*			0.58	*0.10*	3.15	*1.25*	0.77	*0.10*	1.25	*0.27*	1.44	*0.17*	1.51	*0.23*
I/Cl · 10^{-6} (molar)	164	*27.4*	53	*8.7*	61.9	*6.4*	24.7	*8.5*			252	*27.9*	65.4	*17.9*	17.7	*1.5*	32.3	*4.7*	22.3	*15.8*	232	*26.7*
$log(f_{HF}/f_{HCl})$	-1.01	*0.09*	-1.62	*0.08*	-1.47	*0.04*	-1.79	*0.11*	-1.69	*0.05*	-0.74	*0.08*	-1.40	*0.12*	-2.28	*0.06*	-1.99	*0.08*	-2.33	*0.06*	-1.46	*0.05*
$log(f_{H2O}/f_{HF})$	4.63	*0.08*	4.94	*0.22*	4.85	*0.25*	5.01	*0.21*	4.92	*0.27*	3.68	*0.73*	4.44	*0.35*	5.92	*0.15*	5.74	*0.23*	5.55	*0.39*	5.79	*0.11*
$log(f_{H2O}/f_{HCl})$	3.63	*0.07*	3.33	*0.19*	3.38	*0.24*	3.22	*0.18*	3.23	*0.25*	*2.97*	*0.68*	*3.04*	*0.34*	3.64	*0.13*	3.75	*0.24*	3.22	*0.38*	4.33	*0.11*

[a] Calculated assuming full (F,Cl,OH) site, and F and Cl data from SIMS when possible.

[b] Ca concentrations calculated based on the ^{42}Ca isotope.

SD = Standard deviation (1σ); <LOD = Below limit of detection; I.STD = Internal standard; N.A. = Not analysed

Figure 1

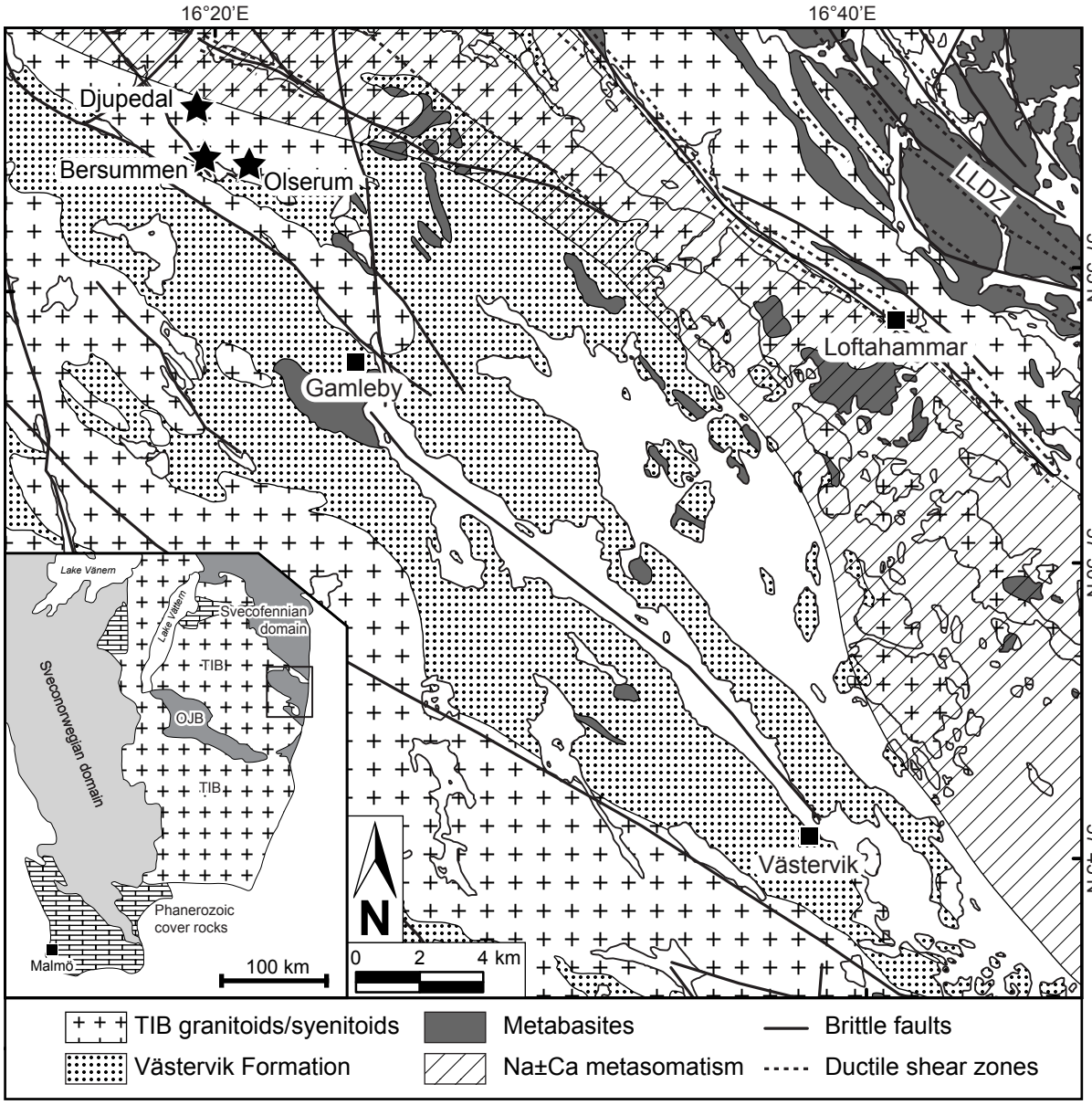

Figure 1 - 2-column figure

Figure 2

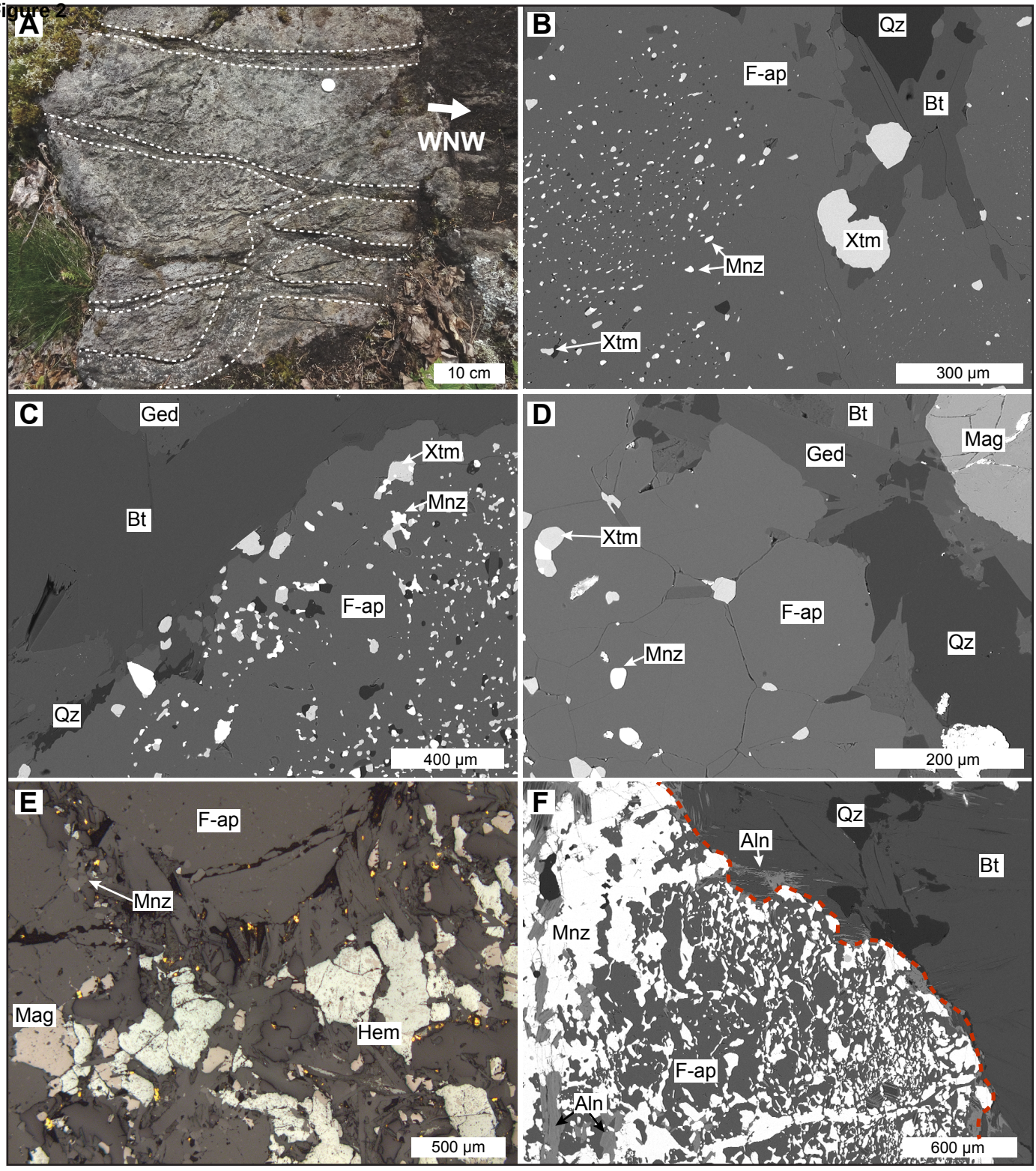

Figure 2 - 2-column figure

Figure 3

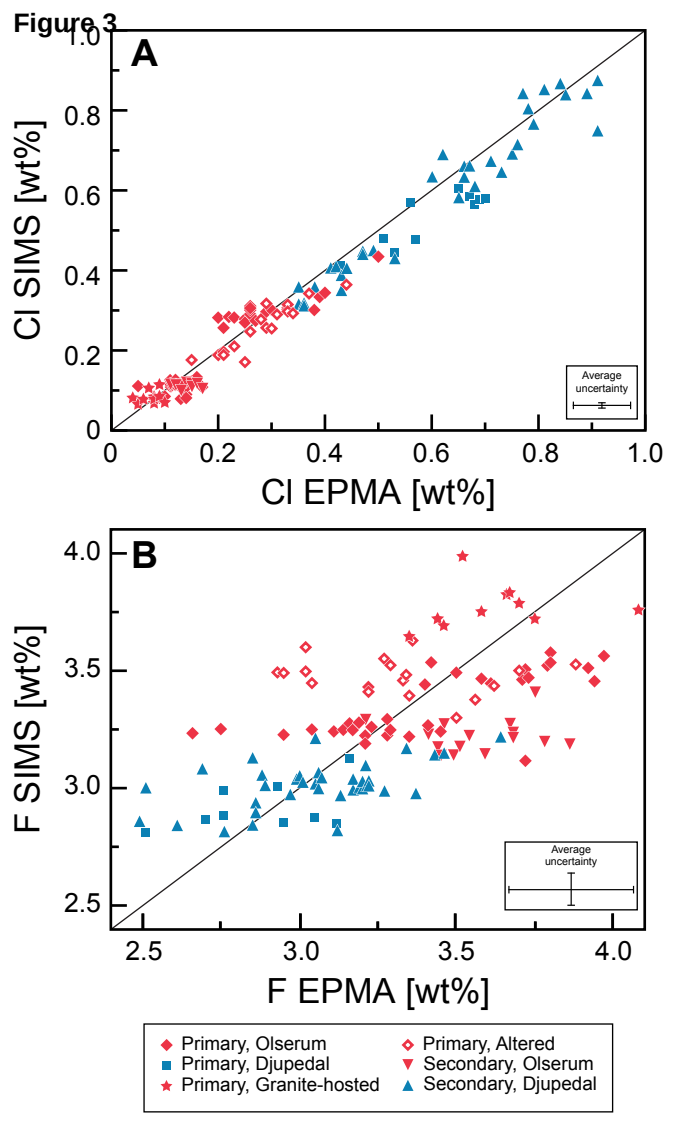

Figure 3 - single-column figure

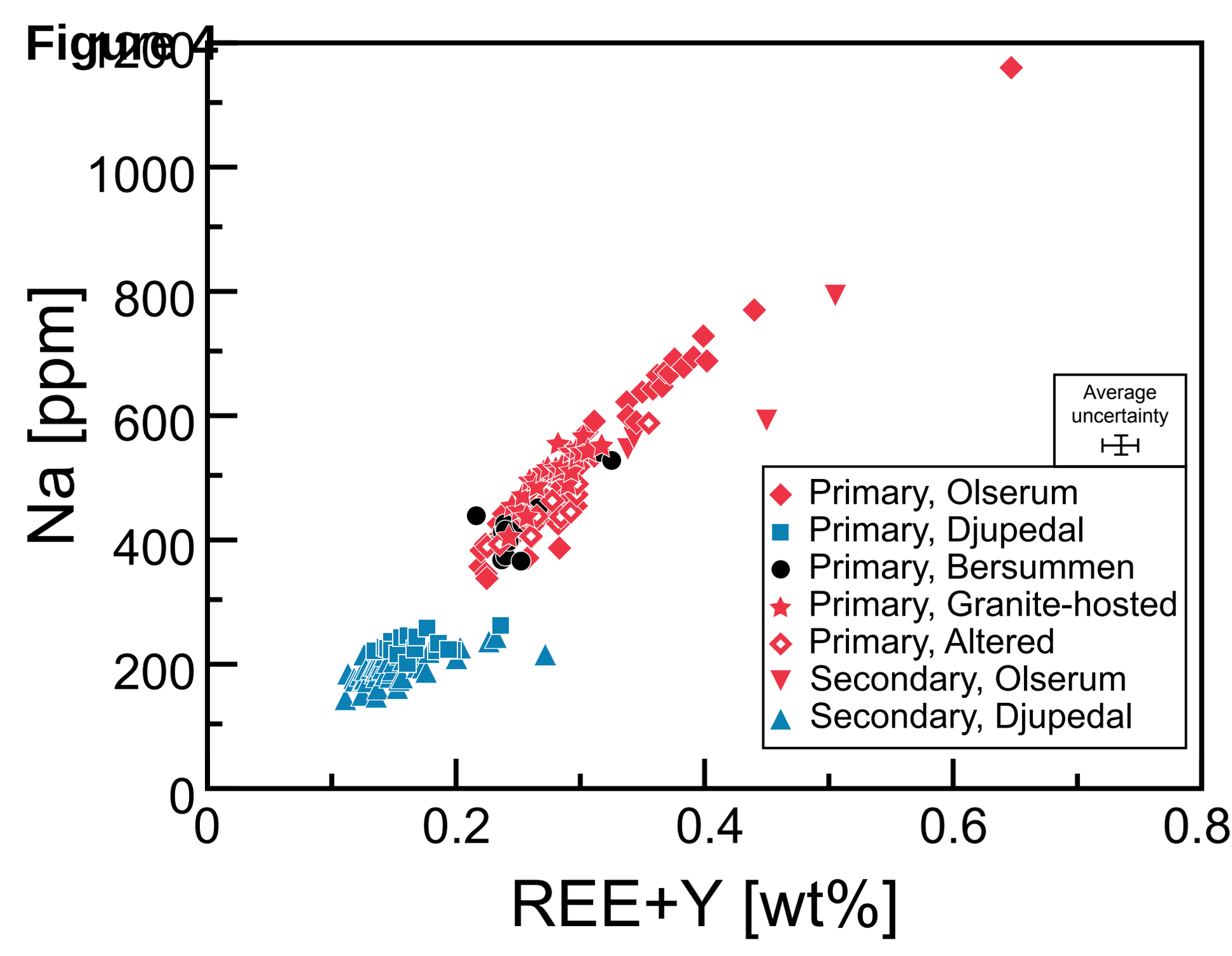

Figure 4 - single column figure

Figure 5

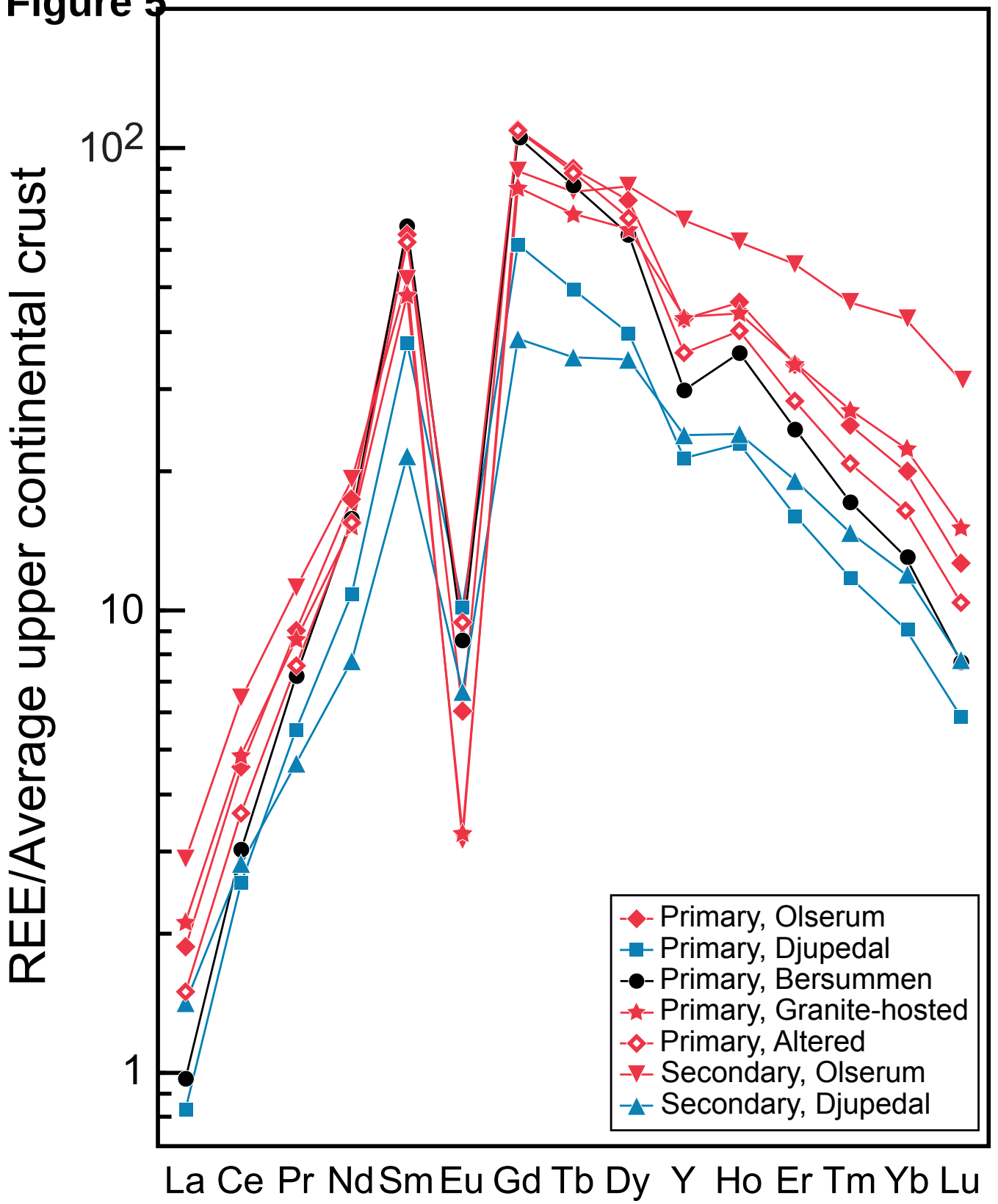

Figure 5 - single-column figure

Figure 6

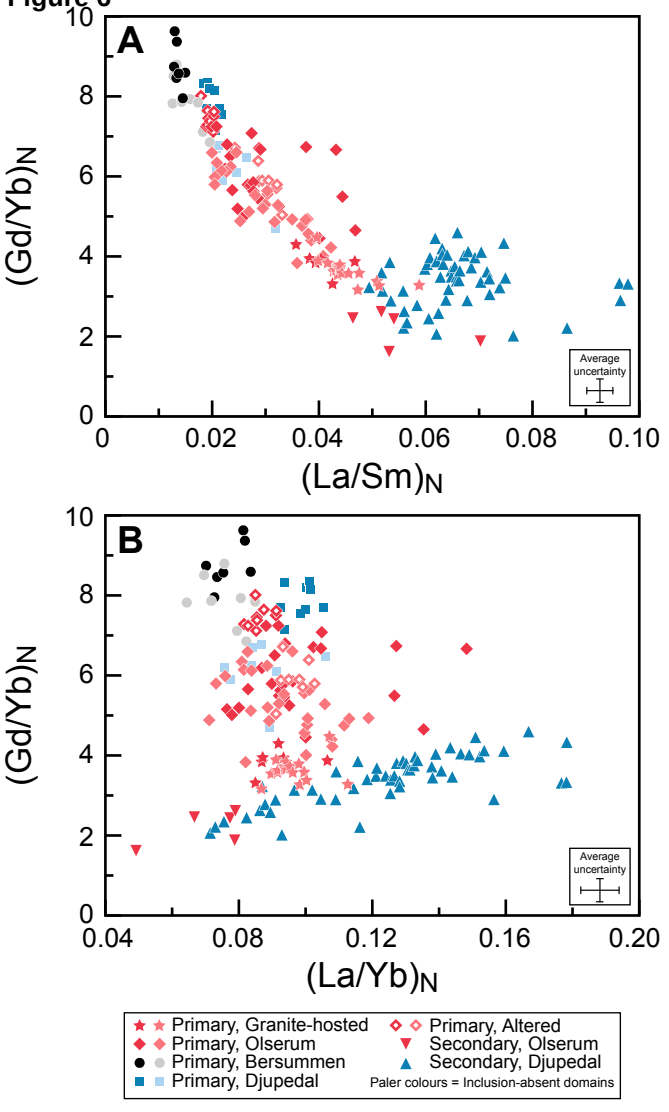

Figure 6 - single-column figure

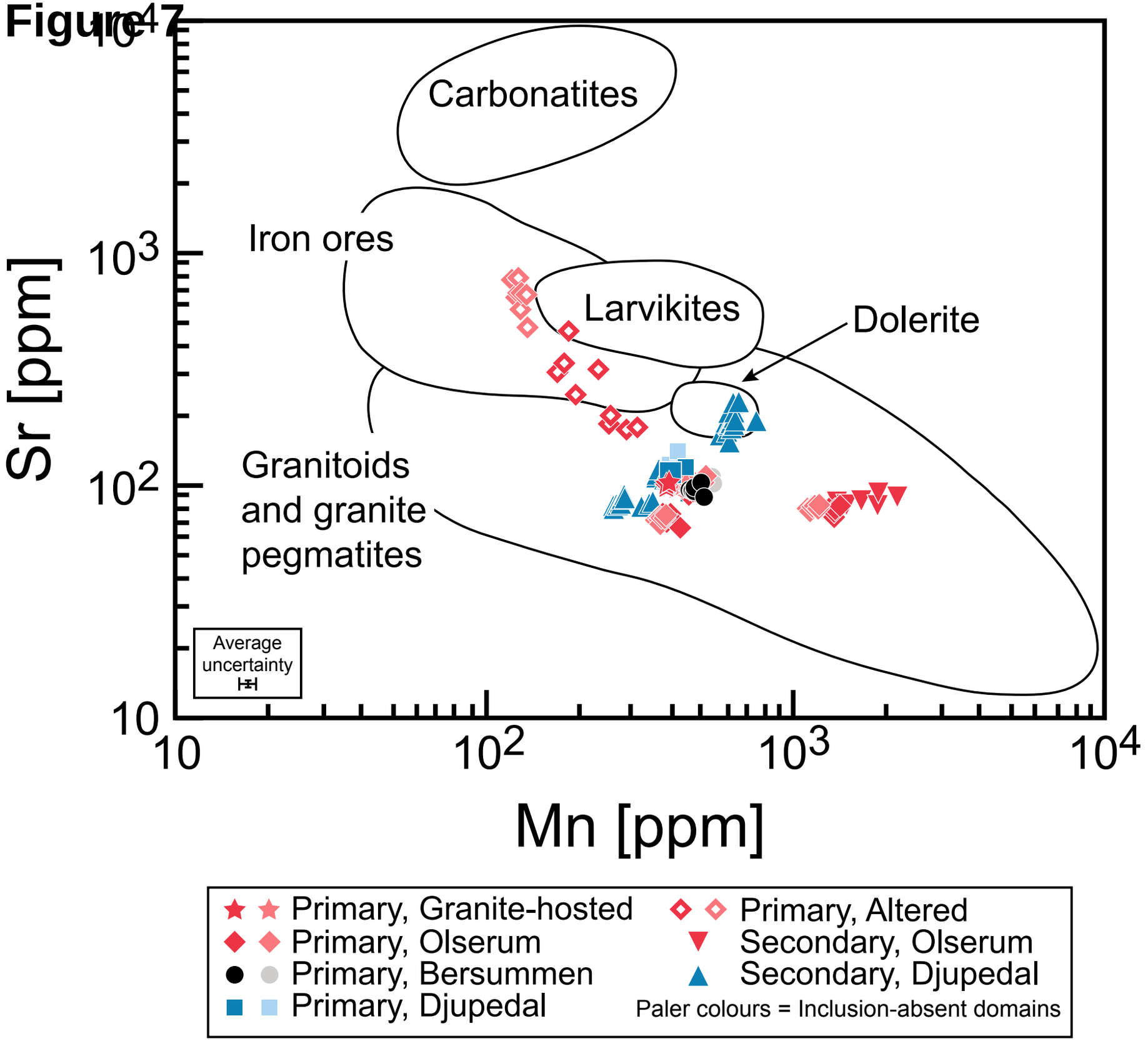

Figure 7 - single column figure

Figure 8

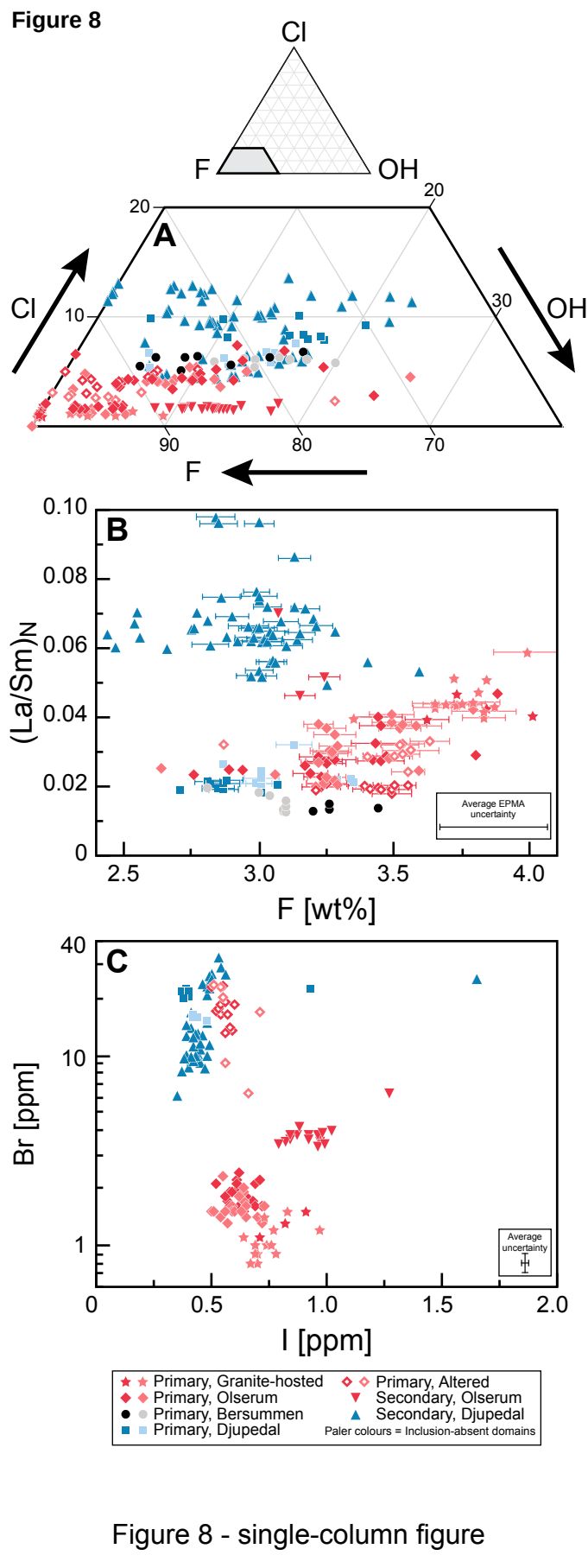

Figure 8 - single-column figure

Figure 9

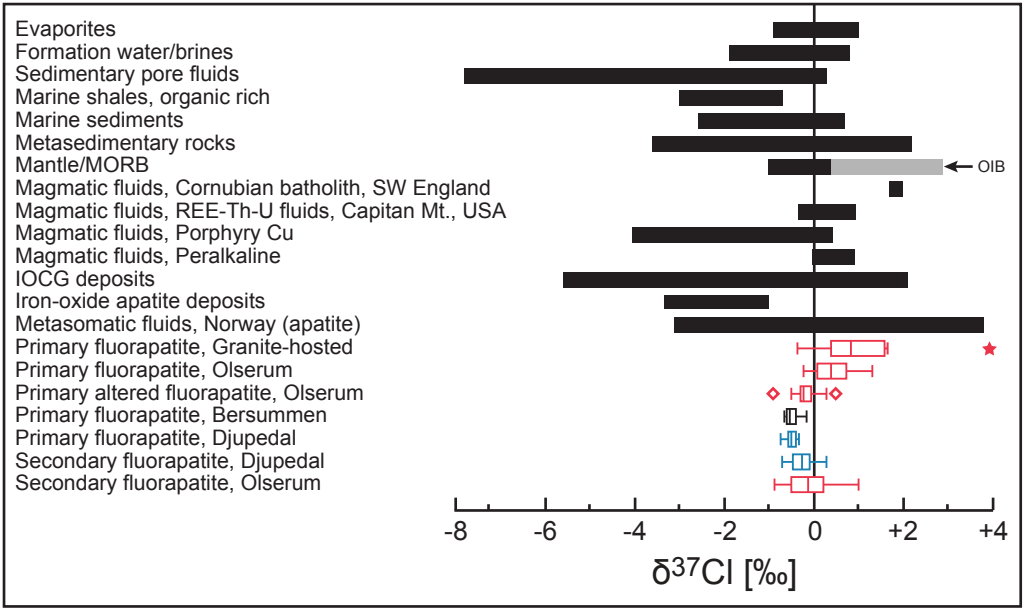

Figure 9 - 1.5-column figure

Figure 10

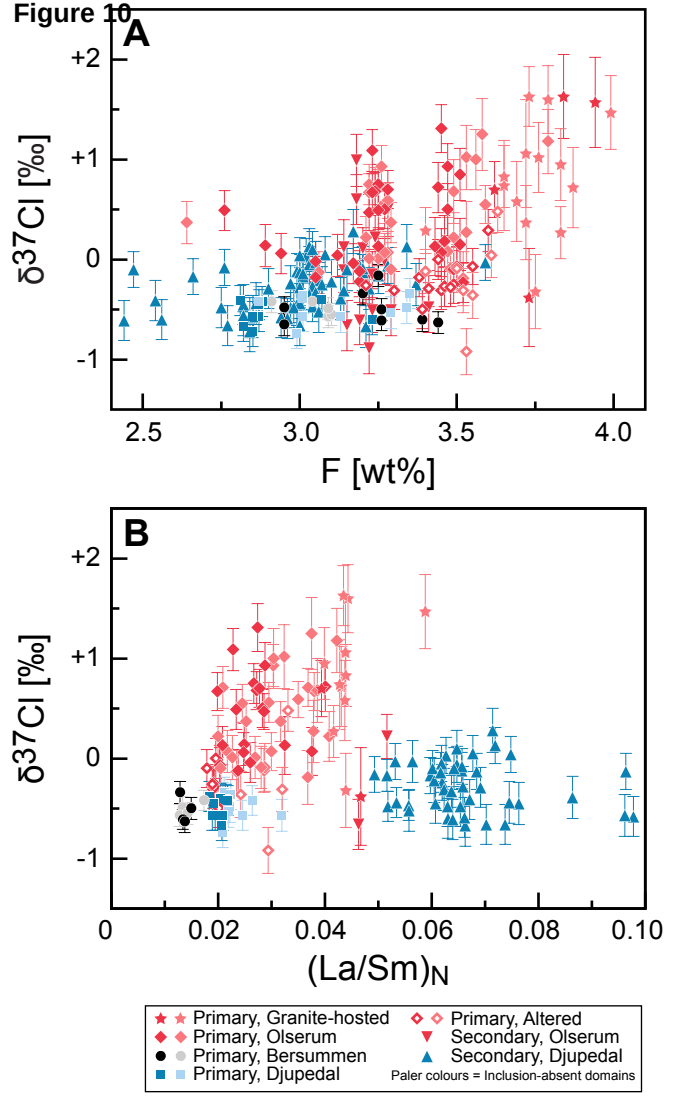

Figure 10 - single-column figure

Figure 11

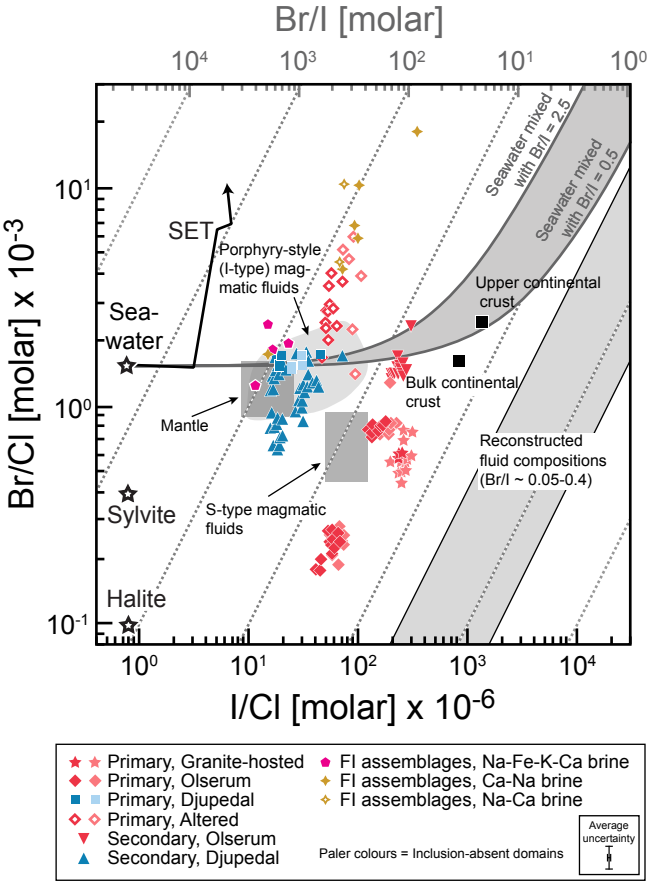

Figure 11 - single-column figure

Figure 12

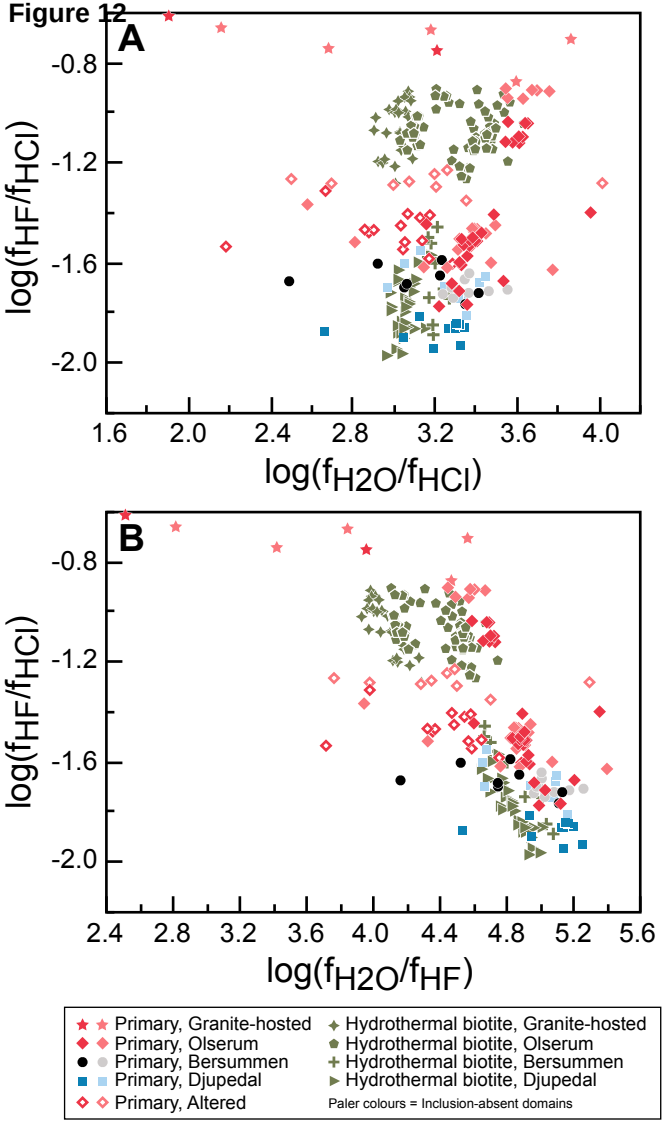

Figure 12 - single-column figure

Figure 13

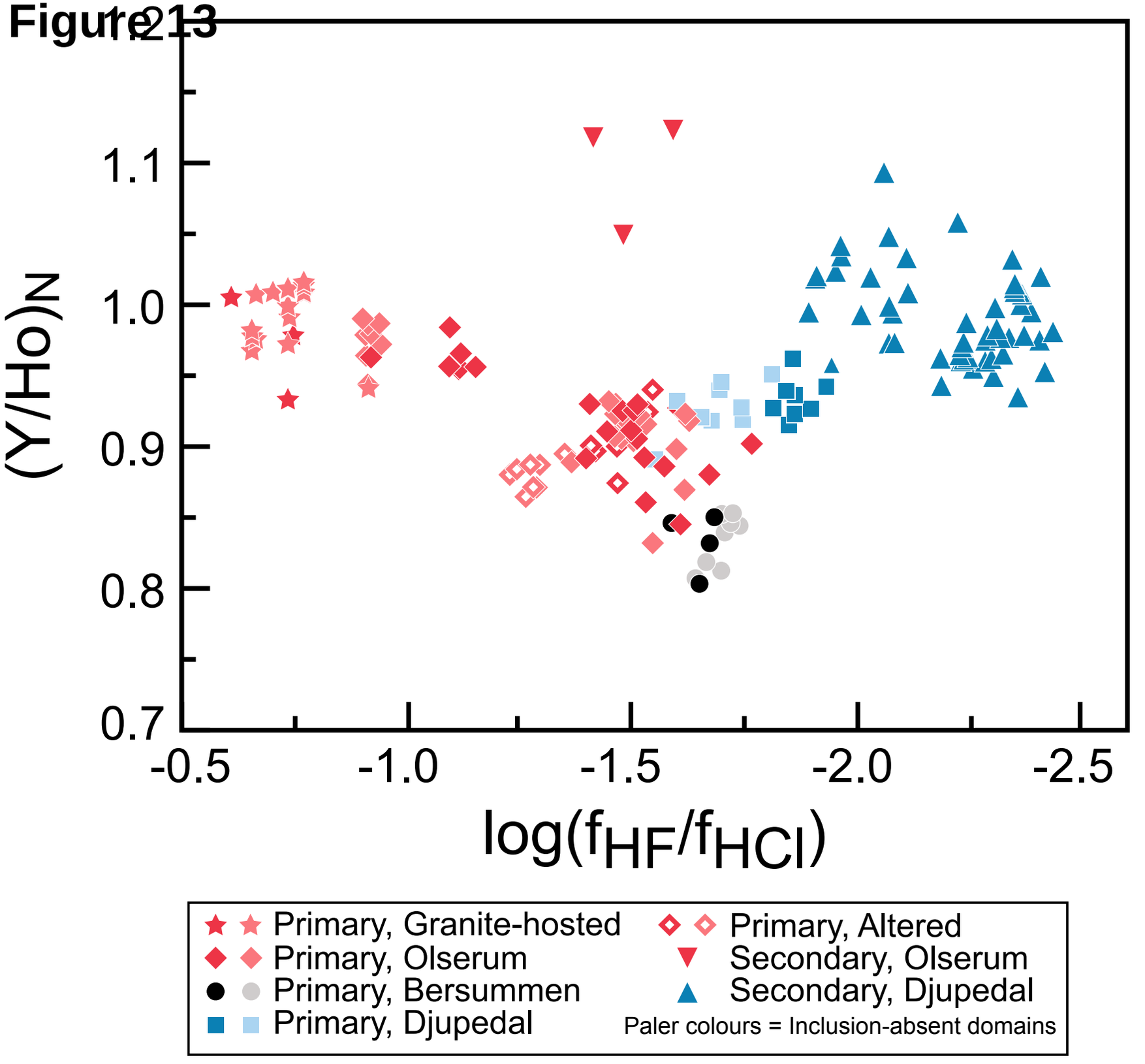

Figure 13 - single-column figure

Figure 14

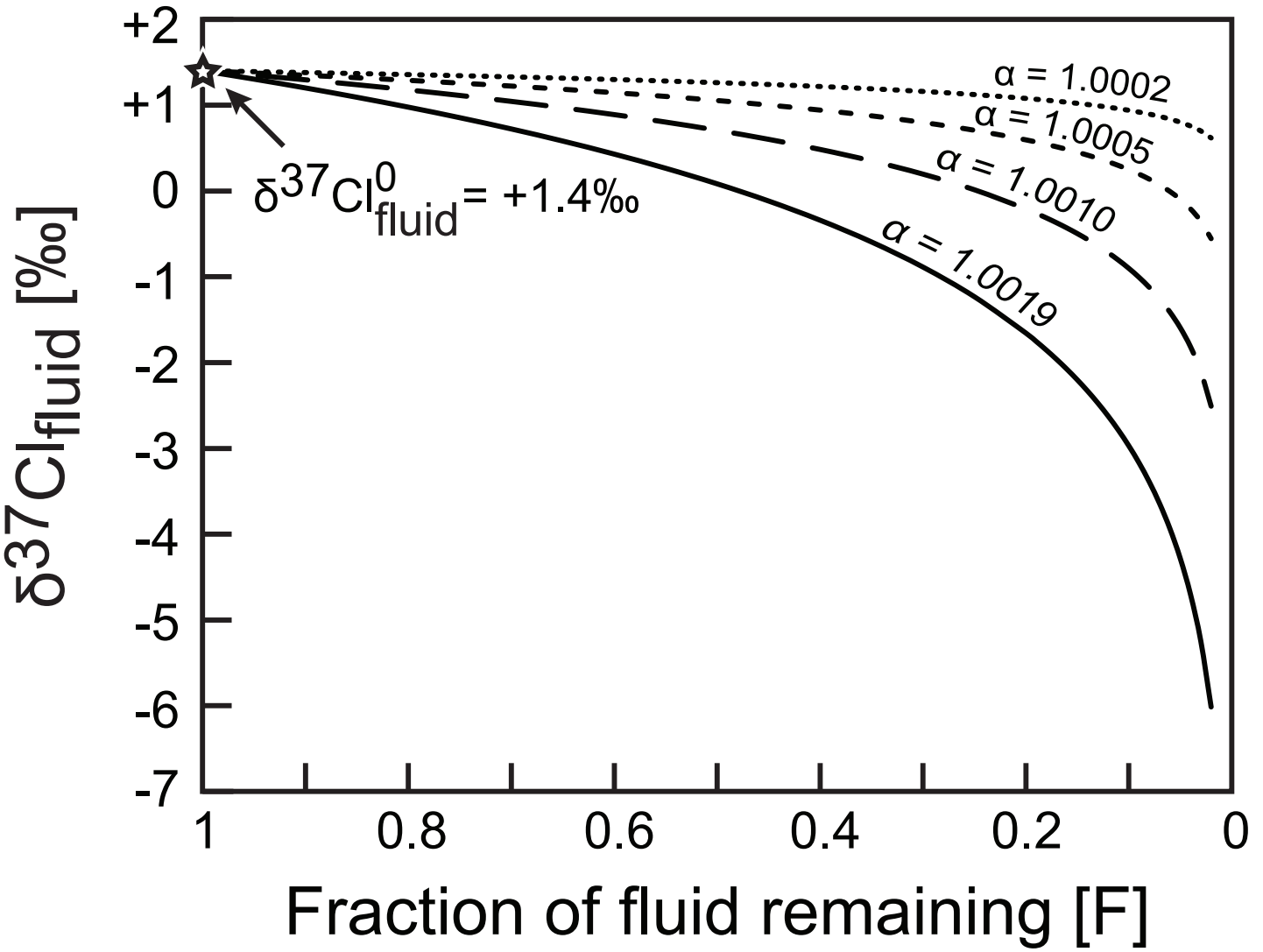

Figure 14 - single-column figure